The Galaxy Activity, Torus, and Outflow Survey (GATOS). II. Torus and polar dust emission in nearby Seyfert galaxies

A. Alonso-Herrero, S. García-Burillo, S. F. Hönig, I. García-Bernete, C. Ramos Almeida, O. González-Martín, E. López-Rodríguez, P. G. Boorman, A. J. Bunker, L. Burtscher, et al.

▶ **To cite this version:**

A. Alonso-Herrero, S. García-Burillo, S. F. Hönig, I. García-Bernete, C. Ramos Almeida, et al.. The Galaxy Activity, Torus, and Outflow Survey (GATOS). II. Torus and polar dust emission in nearby Seyfert galaxies. Astronomy and Astrophysics - A&A, 2021, 652, 10.1051/0004-6361/202141219 . insu-03713767

HAL Id: insu-03713767

https://insu.hal.science/insu-03713767

Submitted on 5 Jul 2022

HAL is a multi-disciplinary open access archive for the deposit and dissemination of scientific research documents, whether they are published or not. The documents may come from teaching and research institutions in France or abroad, or from public or private research centers.

L'archive ouverte pluridisciplinaire **HAL**, est destinée au dépôt et à la diffusion de documents scientifiques de niveau recherche, publiés ou non, émanant des établissements d'enseignement et de recherche français ou étrangers, des laboratoires publics ou privés.

A&A 652, A99 (2021)
https://doi.org/10.1051/0004-6361/202141219
© ESO 2021

Astronomy & Astrophysics

The Galaxy Activity, Torus, and Outflow Survey (GATOS)

II. Torus and polar dust emission in nearby Seyfert galaxies

A. Alonso-Herrero[1], S. García-Burillo[2], S. F. Hönig[3], I. García-Bernete[4], C. Ramos Almeida[5,6], O. González-Martín[7], E. López-Rodríguez[8], P. G. Boorman[9], A. J. Bunker[4], L. Burtscher[10], F. Combes[11], R. Davies[12], T. Díaz-Santos[13], P. Gandhi[3], B. García-Lorenzo[5,6], E. K. S. Hicks[14], L. K. Hunt[15], K. Ichikawa[12,16,17], M. Imanishi[18,19,20], T. Izumi[21], A. Labiano[1], N. A. Levenson[23], C. Packham[24,18], M. Pereira-Santaella[22], C. Ricci[25,26], D. Rigopoulou[4], P. Roche[4], D. J. Rosario[27], D. Rouan[28], T. Shimizu[12], M. Stalevski[29,30], K. Wada[31,32,33], and D. Williamson[3]

(Affiliations can be found after the references)

Received 30 April 2021 / Accepted 30 June 2021

ABSTRACT

We compare high angular resolution mid-infrared (mid-IR) and Atacama Large Millimeter/submillimeter Array (ALMA) far-infrared (far-IR) images of twelve nearby (median 21 Mpc) Seyfert galaxies selected from the Galaxy Activity, Torus, and Outflow Survey (GATOS). The mid-IR unresolved emission contributes more than 60% of the nuclear (diameters of 1.5″ ∼ 150 pc) emission in most galaxies. By contrast, the ALMA 870 μm continuum emission is mostlyresolved with a median diameter of 42 pc and typically along the equatorial direction of the torus (Paper I). The Eddington ratios and nuclear hydrogen column densities ($N_{\rm H}$) of half the sample are favorable to launching polar and/or equatorial dusty winds, according to numerical simulations. Six of these show mid-IR extended emission approximately in the polar direction as traced by the narrow line region and perpendicular to the ALMA emission. In a few galaxies, the nuclear $N_{\rm H}$ might be too high to uplift large quantities of dusty material along the polar direction. Five galaxies have low $N_{\rm H}$ and/or Eddington ratios and thus polar dusty winds are not likely. We generated new radiative transfer CAT3D-WIND disk+wind models and model images at 8, 12, and 700 μm. We tailored these models to the properties of the GATOS Seyferts in this work. At low wind-to-disk cloud ratios, the far-IR model images have disk- and ring-like morphologies. The characteristic "X"-shape associated with dusty winds is seen better in the far-IR at intermediate-high inclinations for the extended-wind configurations. In most of the explored models, the mid-IR emission mainly comes from the inner part of the disk and cone. Extended biconical and one-sided polar mid-IR emission is seen in extended-wind configurations and high wind-to-disk cloud ratios. When convolved to the typical angular resolution of our observations, the CAT3D-WIND model images reproduce qualitative aspects of the observed mid- and far-IR morphologies. However, low to intermediate values of the wind-to-disk ratio are required to account for the observed large fractions of unresolved mid-IR emission in our sample. This work and Paper I provide observational support for the torus+wind scenario. The wind component is more relevant at high Eddington ratios and/or active galactic nucleus luminosities, and polar dust emission is predicted at nuclear column densities of up to $\sim 10^{24}$ cm^{-2}. The torus or disk component, on the other hand, prevails at low luminosities and/or Eddington ratios.

Key words. galaxies: Seyfert – submillimeter: galaxies – infrared: galaxies – galaxies: ISM

1. Introduction

The fundamental component of the unified model for active galactic nuclei (AGN) is an obscuring torus or disk[1] made of dust and molecular gas (see Antonucci 1993; Urry & Padovani 1995; Netzer 2015, for reviews). In the classical scenario, the torus obscures the view of the broad line region (BLR) along certain lines of sight and the nuclei are classified as type 2. Those nuclei observed along or near the polar direction of the torus have a direct view of the BLR and are classified as type 1. Initially, Pier & Krolik (1993) derived a compact size (a few parsecs) for the torus of the archetypical Seyfert 2 galaxy NGC 1068, from the fit of the infrared (IR) spectral energy distribution (SED) with the torus models of Pier & Krolik (1992a). Subsequent modeling of a sample of Seyfert 1s by Granato & Danese (1994), however, required tori extending for up to a few hundred parsecs. The narrow line region (NLR) of Seyfert galaxies extends on much larger scales (hundreds of parsecs up to approximately a kiloparsec) than the dusty molecular torus and is thus seen in both type 1 and type 2 AGN.

The angular resolutions needed in the IR to resolve the obscuring structures of nearby AGN have not been available until recently. In the mid-infrared[2] (mid-IR), interferometric observations with the Very Large Telescopes Interferometer (VLTI) of nearby Seyferts are generally modeled with an unresolved source and a resolved source. Both show compact sizes (∼1−10 pc, Burtscher et al. 2013; López-Gonzaga et al. 2016). Some of the resolved model components are elongated in the polar direction, with this component accounting for most of the mid-IR emission on these scales (Hönig et al. 2013; Tristram et al. 2014; López-Gonzaga et al. 2014, 2016; Leftley et al. 2019). This polar dust emission appears to be related to the large scale (up to a few hundred parsec) emission detected in the mid-IR (Cameron et al. 1993; Tomono et al. 2001; Radomski et al. 2003; Packham et al. 2005a; Asmus et al. 2014; Asmus 2019; García-Bernete et al. 2016) and with SOFIA at 30 μm (see Fuller et al. 2019). In many local Seyferts that

[1] Throughout this work we use the terms torus and nuclear disk interchangeably. In particular, unless otherwise indicated, the term torus does not necessarily refer to a geometrically thick one, which is defined as having a height over radial size ratio of $H/R = 1$.

[2] Throughout this work, mid-IR refers to the ∼7−26 μm spectral range that can be observed from the ground.

is spatially coincident with that of the NLR and/or ionization cones. In the near-infrared (near-IR) GRAVITY Collaboration (2020a) reconstructed VLT/GRAVITY K-band observations of NGC 1068 with a ring-like structure with a radius of 0.24 pc. This emission is believed to be associated with the dust sublimation region but, according to these authors, the geometry is not consistent with that expected from a geometrically thick torus. Furthermore, for a sample of Seyfert 1s, GRAVITY Collaboration (2020b) resolved the radii of the hot dust continuum emission and showed they follow the luminosity-size relation (Suganuma et al. 2006; Kishimoto et al. 2007), as expected for the dust sublimation region.

Observations with the Atacama Large Millimeter/submillimeter Array (ALMA) of NGC 1068 resolved the far-infrared (far-IR) or submillimeter continuum emission of the torus (García-Burillo et al. 2016, 2019; Lopez-Rodriguez et al. 2020). At 432 µm the torus diameter is 7−10 pc. The derived (sub)millimeter spectral indices at the AGN position of NGC 1068 indicate the presence of cold dust but with an important contribution from synchrotron emission at these wavelengths (García-Burillo et al. 2019; Pasetto et al. 2019). The torus was also detected in a variety of molecular gas transitions that probe a range of gas densities with the torus diameter reaching ∼30 pc in the low density tracers (see García-Burillo et al. 2016, 2019; Gallimore et al. 2016; Impellizzeri et al. 2019; Imanishi et al. 2020).

Molecular tori with diameters of up to 50 pc are now routinely observed with ALMA in other nearby Seyfert galaxies and low luminosity AGN. The tori are sometimes morphologically and kinematically decoupled from the host galaxy. However, in most cases the tori are connected to reservoirs of molecular gas on scales of ∼100 pc that are associated with dynamical resonances (see Izumi et al. 2018; Alonso-Herrero et al. 2018, 2019; Combes et al. 2019, and also below). These reservoirs are likely related to the 100 pc-torus invoked by Maiolino & Rieke (1995) to explain the properties of 1.8 and 1.9 Seyfert nuclei. These would be type 1s seen through these large scale dust structures that are coplanar with the host galaxy disk. Finally there is evidence that in some cases the torus itself is not only rotating but also outflowing (Gallimore et al. 2016; Alonso-Herrero et al. 2018; García-Burillo et al. 2019).

In parallel with the new observational constraints on the torus properties, theoretical models are continuously evolving. In the first static models the dust was homogeneously distributed (Pier & Krolik 1992a; Granato & Danese 1994; Efstathiou & Rowan-Robinson 1995; Fritz et al. 2006). Subsequently, the dust was distributed in clouds in the so-called clumpy torus models (Nenkova et al. 2008a,b; Schartmann et al. 2008; Hönig & Kishimoto 2010) and in two phases (Stalevski et al. 2012; Siebenmorgen et al. 2015). Torus models also incorporated an additional polar dust component to account for the mid-IR imaging and interferometric observations of some Seyfert galaxies (Efstathiou et al. 1995; Gallagher et al. 2015; Hönig & Kishimoto 2017; Stalevski et al. 2017; Isbell et al. 2021). These models reproduced satisfactorily the observed nuclear IR emission of samples of nearby AGN (see e.g., Ramos Almeida et al. 2009, 2011; Alonso-Herrero et al. 2011; Ichikawa et al. 2015; García-González et al. 2017; García-Bernete et al. 2019; González-Martín et al. 2019). Elitzur & Shlosman (2006) put forward a scenario where the torus is part of a clumpy outflow, and recently Venanzi et al. (2020) demonstrated theoretically that dusty winds can be launched at the inner walls of the torus. Radiation hydrodynamical models (Schartmann et al. 2014; Wada et al. 2016; Williamson et al. 2019, 2020) incorporated predictions for the dust IR emission and the molecular gas emission and kinematics.

Hönig (2019) assembled the information gathered from the analysis of IR and submm data of nearby and bright AGN and proposed a new paradigm for the obscuring structures around radio-quiet AGN (see also Ramos Almeida & Ricci 2017; Lyu & Rieke 2021). The torus is now envisioned as a multicomponent multiphase structure (see Figs. 1 and 4 from Izumi et al. 2018; Hönig 2019, for schematic pictures, respectively). In short, the hot innermost part of the equatorial disk or torus is close to the sublimation radius on subparsec scales in Seyferts and emits mostly in the near-IR. The dusty inner molecular torus as well as the wind region are traced by the mid-IR emission as well as hot and relatively warm molecular gas on scales of a few pc to probably tens of parsecs. Both dust components (that is, the inner molecular disk and the wind) are likely to contribute to the AGN obscuration. Finally, the cold outer part of the equatorial disk is probed by the cold molecular gas and dust emission and extends on scales from 5 pc out to tens of parsecs.

This is the second paper in a series aimed at understanding the nuclear activity and its connection with the host galaxy in nearby Seyfert galaxies. In the first paper of the series, Garcia-Burillo et al. (2021), GB21 from now on, obtained ALMA observations of a volume-limited and complete sample of Seyfert galaxies to study their torus properties. The galaxies are part of the Galactic Activity, Torus, and Outflow Survey (GATOS). We drew the GATOS galaxies from the 70 Month *Swift*-BAT All-sky Hard X-ray Survey (Baumgartner et al. 2013). The *Swift*-BAT 14−195 keV energy range ensures a nearly complete selection for nearby AGN at $L_{\rm AGN}$ (14−150 keV) > 10^{42} erg s^{-1} (Ricci et al. 2017a; Koss et al. 2017). GB21 selected galaxies in the southern hemisphere and with distances in the 10−40 Mpc range. We summarize the main properties of the sample of 12 Seyfert galaxies in Table 1. The median galaxy distance is 21 Mpc and the median value of the intrinsic (absorption corrected) 2−10 keV luminosity is 2×10^{42} erg s^{-1}. The Eddington ratios ($\lambda_{\rm Edd}$) vary from 0.001 to 0.06. The sample probes a range of X-ray column densities and includes two Compton-thick objects.

In this paper we characterize for the first time the torus and polar dust emission components in nearby Seyferts, using mid and far-IR observations with physical resolutions 7−50 pc. The paper is organized as follows. We describe the existing mid-IR observations with angular resolutions 0.2−0.4″ in Sect. 2.1. We summarize in Sect. 2.2 the ALMA observations analyzed and discussed in detail by GB21. In Sect. 3 we derive the extended mid-IR emission of our Seyfert galaxies, and compare it with ALMA and NLR observations. In Sect. 4 we investigate the mid-IR morphology dependence on AGN properties. In Sect. 5 we generate mid- and far-IR torus model images using the disk+wind models of Hönig & Kishimoto (2017). In Sect. 6 we use these model images to simulate our observations. Sections 7 and 8 present the discussion and summary, respectively.

2. Observations

The observations used in this work have already been presented in the literature. In what follows we describe them briefly.

2.1. Mid-IR observations

We used fully-reduced mid-IR imaging observations taken with 8−10 m class telescopes and already published in the literature

Table 1. Sample.

Galaxy	Dist (Mpc)	Type	log L (2−10 keV) (erg s^{-1})	X-ray log N_H (cm^{-2})	log λ_{Edd}	ALMA log N_{H2} (cm^{-2})
NGC 1365	18.3	Sy1.8	42.09	22.2	−1.6	22.3
NGC 3227	23.0	Sy1.5	42.37	21.0	−1.2	22.7
NGC 4388	18.1	Sy1.9	42.45	23.5	−1.2	22.3
NGC 4941	20.5	Sy2	41.40	23.7	−2.4	21.9
NGC 5506	26.4	Sy1.9	42.98	22.4	−2.3	22.6
NGC 5643	16.9	Sy2	42.41	25.4	−1.3	23.6
NGC 6300	14.0	Sy2	41.73	23.5	−1.9	23.4
NGC 6814	22.8	Sy1.5	42.24	21.0	−1.6	≤21.8
NGC 7213	22.0	Sy1.5	41.85	20.0	−3.0	≤22.0
NGC 7314	17.4	Sy1.9	42.18	21.6	−1.2	22.1
NGC 7465	27.2	Sy2	41.93	21.5	−2.2	22.7
NGC 7582	22.5	Sy2	43.49	24.3	−1.7	22.6

Notes. The distances are from the NASA/IPAC Extragalactic Database (NED) for $H_0 = 73\,\mathrm{km\,s^{-1}\,Mpc^{-1}}$, $\Omega_m = 0.27$, and $\Omega_\Lambda = 0.73$. The Seyfert types are taken from Véron-Cetty & Véron (2006), except for NGC 7213, which is taken from Phillips (1979). The absorption corrected 2−10 keV luminosities and X-ray column densities are from Ricci et al. (2017a). The Eddington ratios (λ_{Edd}) are from Koss et al. (2017) except for NGC 1365, which is from Vasudevan et al. (2010). The H_2 column densities are based on ALMA CO(3−2) estimates at the AGN position from GB21.

Table 2. Mid-IR observations and analysis.

Galaxy	Tel./Inst.	Filter	λ_c (μm)	*FWHM* (″)	*FWHM* (pc)	Ref.	Unresolv. (%)	$PA_{MIR-ext}$ (°)	Morphology
NGC 1365	Gemini-S/T-ReCS	Si-2	8.74	0.34	30	1	57	−65 to −70	Unresolv. plus two-sided polar
NGC 3227	GTC/CanariCam	Si-2	8.74	0.31	35	2	69	30 to 45	Unresolv. plus one-sided polar
NGC 4388	GTC/CanariCam	Si-2	8.74	0.39	34	2	72	30	Unresolv. plus one-sided polar
NGC 4941	VLT/VISIR	NeII-1	12.27	0.35	35	3	∼100	...	Unresolved
NGC 5506	VLT/VISIR	NeII-1	12.27	0.33	42	3	61	30 to 90	Unresolv. plus polar plus equatorial/host
NGC 5643	VLT/VISIR(u)	B12.4	12.47	0.34	28	4	53	48 to 70	Unresolv. plus polar plus equatorial/host
NGC 6300	VLT/VISIR	PAH1	8.59	0.25	17	3	36	−65 to −76	Unresolv. plus equatorial/host
NGC 6814	VLT/VISIR	PAH2	11.25	0.35	39	3	78	...	Unresolved
NGC 7213	VLT/VISIR(u)	PAH1	8.59	0.26	28	5	∼100	...	Unresolved
NGC 7314	Gemini-S/T-ReCS	Si-2	8.74	0.37	31	6	67	...	Unresolved
NGC 7465	GTC/CanariCam	Si-2	8.74	0.38	50	2	80	...	Unresolved
NGC 7582	VLT/VISIR(u)	B12.4	12.47	0.36	40	4	70	45 to 55	Unresolv. plus one-sided polar

Notes. The FWHM of the observations are measured by fitting a 2D Gaussian to the standard star images taken close in time to the galaxy observations. Fully reduced images are from: 1. Alonso-Herrero et al. (2012). 2. Alonso-Herrero et al. (2016). 3. Asmus et al. (2014). 4. Asmus (2019). 5. Leftley et al. (2019). 6. García-Bernete et al. (2016). The unresolved flux fraction is measured within 1.5−1.6″ diameter apertures. When two values for $PA_{MIR-ext}$ (see Sect. 3) are given, the first one corresponds to the inner regions and the second to the outer regions within approximately 1″.

(see references in Table 2). The instruments included VISIR (Lagage et al. 2004) and the upgraded VISIR (Käufl et al. 2015; Kerber et al. 2016) on the VLT, T-ReCS (Telesco et al. 1998) on Gemini-South (Gemini-S), and CanariCam (Telesco et al. 2003; Packham et al. 2005b) on the Gran Telescopio Canarias (GTC). We used observations taken with various filters in the atmospheric N-band listed in Table 2.

For each galaxy, we also obtained fully-reduced images of standard stars taken with the same filter and observed close in time. All the observations have angular resolutions, as measured from the full width at half maximum (FWHM) of the stars, close to the theoretical diffraction limit of the corresponding telescopes in the mid-IR (0.2−0.4″). At the distances of our galaxies, these correspond to physical resolutions between 17 pc for NGC 6300 and 50 pc for NGC 7465. The pixel sizes are as follows, 0.0453″ for the upgraded VISIR, 0.075″ for VISIR, 0.0798″ for CanariCam and 0.09″ for T-ReCS.

We note that the observations from the atlas of Asmus et al. (2014) were already at the usual orientation of north up, east to the left. The T-ReCS and CanariCam original images had different orientations and we kept them during the point spread function (PSF) subtraction analysis (see Sect. 3), and only rotated them to the usual orientation after the PSF subtraction. We refer the reader to the works listed in the notes of Table 2 for full details on the observations and data reduction.

2.2. ALMA CO(3−2) and continuum 870 μm observations

We obtained ALMA band 7 (frequency range 275−373 GHz, wavelength range 0.8−1.1 mm) observations of the GATOS core sample of 10 Seyferts in Cycles 6 and 7. We targeted the CO(3−2) and HCO^+(4−3) transitions as well as the adjacent continuum at 870 μm with a common angular resolution of 0.1″, which translates into physical resolutions in the range 7−10 pc for our sample. GB21 presented the observations, data

reduction, and analysis. For this work, we use the fully reduced maps of the 870 μm continuum and integrated intensity CO(3−2) (see Sect. 3.3) generated from their moderate spatial resolution (MSR) data sets as well as the torus properties derived from the modeling of the MSR 870 μm continuum (see Sect. 3.3). The ALMA band 7 observations of the other two galaxies in our sample, namely NGC 1365 and NGC 3227, were part of other ALMA programs and were published by Combes et al. (2019) and Alonso-Herrero et al. (2019), respectively.

3. Extended mid-IR emission

3.1. Analysis of the observations

The nuclear mid-IR emission of nearby active galaxies, as observed from ground-based telescopes, is a combination of an unresolved component, generally assumed to arise from dust heated by the AGN, and extended emission. The latter arises from dust in the NLR and/or dust heated by ongoing star formation activity, especially in local Seyferts that are also classified as luminous IR galaxies (see the review by Pérez-Torres et al. 2021, and references therein), or might be due to synchrotron emission, especially in radio-loud low-luminosity AGN (Mason et al. 2012).

To separate the unresolved and extended emission from ground-based mid-IR images, the majority of works used the so-called PSF-scaling technique. The main assumption is that an imaging observation of a standard star taken close in time to the galaxy observation represents the galaxy unresolved nuclear component. The standard star image is then scaled to the peak of the galaxy observation and subtracted from the galaxy image. The scaling level (that is, 100%, 90%, etc. at the peak of the galaxy emission) is visually assessed from the PSF-subtracted image and the azimuthally averaged one-dimension (1D) emission profiles (see, e.g., Fig. 1 in Radomski et al. 2003; Ramos Almeida et al. 2011). Generally in Seyfert galaxies a 100% scaling produces residual holes at the center of the galaxy and the scaling level is determined when the residual image does not show a central hole and the PSF-subtracted galaxy profile is flat in the central region.

In this work we used the same PSF-scaling technique but we first determined the scaling factor by fitting 1D emission profiles. We extracted 1D profiles of one pixel width, centered at the peak of the emission along each of the X and Y axes of the mid-IR galaxy and standard star images. We used the original images before rotating to the usual orientation and smoothing them. We started by fitting separately the X and Y profiles of the corresponding standard stars with one Gaussian function to derive the width σ of the unresolved component. We then used two Gaussians for the galaxy profiles along each of the X and Y directions. The first component models the unresolved component. We fixed its σ to the value derived from the standard star (within ±1 pixel), and allowed its intensity and position to vary. For the second Gaussian we allowed all the parameters to vary to model the extended emission. We derived the scaling factors for the unresolved component Gaussian along the X and Y directions. We scaled the PSF images (that is, the standard star images) with the two factors and subtracted them from the galaxy images. From the two PSF-subtracted galaxy images, we chose the one that did not over-subtract the unresolved emission. We note that there is not a strong dependence of the morphology of the extended mid-IR emission with the scaling factor, except in the very inner regions. Asmus (2019) illustrated this in their Fig. 4 for NGC 5643, which is included in our analysis.

Figure 1 shows two examples of the fits to the X and Y direction profiles. The top panels are for NGC 6300, a galaxy in our sample with a large mid-IR extended component and the bottom panels NGC 7213, which appears unresolved in our mid-IR image. In the case of NGC 6300, the 1D profiles show that the extended emission is more prominent along the X-direction (east-west direction in this case) than along the Y-direction. The derived scaling factors were 63% and 84% for the X and Y directions, respectively. The PSF-subtracted galaxy image using the scaling factor along the Y direction had negative residuals and thus we used the scaling factor along the X direction to produce the PSF-subtracted galaxy image. For NGC 7213, both 1D profiles extracted along the X and Y directions were well modelled with a dominant unresolved component, which resulted in a scaling factor of the PSF image of 97−98%.

3.2. Results

In Fig. 2 we display for each galaxy in our sample the original mid-IR image and the resulting PSF-subtracted images for a field of view (FoV) of 2″ × 2″. This FoV includes most of the mid-IR extended emission detected for our sample with the instruments listed in Table 2. The only exceptions are NGC 3227 and NGC 7582 which show extended emission over larger scales due to the presence of circumnuclear rings of star formation (Alonso-Herrero et al. 2016; Wold & Galliano 2006; García-Bernete et al. 2016). We also smoothed the images using Gaussian functions with FWHM of between 1.1 and 1.7 pixels, corresponding to 0.07 to 0.13″. In all the images, the first contour shown with a solid line is at a $3 \times \sigma_{bk}$ level, where σ_{bk} is the standard deviation of the background measured on the original images, that is, before we smoothed the images and when needed, rotated them. The other contours are shown at 5, 10, 15, and $20 \times \sigma_{bk}$ levels.

The PSF-subtracted images of six out of the twelve galaxies present bright extended mid-IR emission (Fig. 2). These are NGC 1365, NGC 3227, NGC 5506, NGC 5643, NGC 6300, and NGC 7582. The contours show that the extended emission is detected up to at least a $20 \times \sigma_{bk}$ level. For NGC 4388 we also detected extended mid-IR emission at a lower significance but in a similar orientation as that derived by Asmus et al. (2016) using a different dataset. The sizes of the extended mid-IR emission range from approximately 50 pc in NGC 6300 to 190 pc in NGC 5506. We used the ellipse task within IRAF on the PSF-subtracted images to derive the position angle (PA) of the extended mid-IR emission ($PA_{MIR-ext}$). The typical uncertainties in these measurements are ±5°. We report these values in Table 2 for the inner ∼1″, which is the location of most of the extended mid-IR emission. $PA_{MIR-ext}$ is relatively constant with radius in NGC 1365, NGC 3227, NGC 4388, NGC 6300, and NGC 7582. For NGC 5643 we found that the values are between approximately 48° in the inner regions (∼0.45″) changing progressively to approximately 60−70° in the outer contours. In the most extreme case in our sample NGC 5506, the $PA_{MIR-ext}$ values vary from 30° in the inner region (central ∼0.5″) to nearly 90° in the outer regions.

Three galaxies, NGC 6814, NGC 7314, and NGC 7465, only show evidence of faint extended emission at $3-5 \times \sigma_{bk}$ levels. Finally, the PSF-subtracted images of NGC 4941 and NGC 7213 do not show evidence of extended emission.

The fraction of unresolved flux over total flux measured within aperture diameters of 1.5−1.6″ (see Table 2) are between 40 and 72% for the seven galaxies with extended mid-IR emission. These apertures cover the extent of the mid-IR nuclear

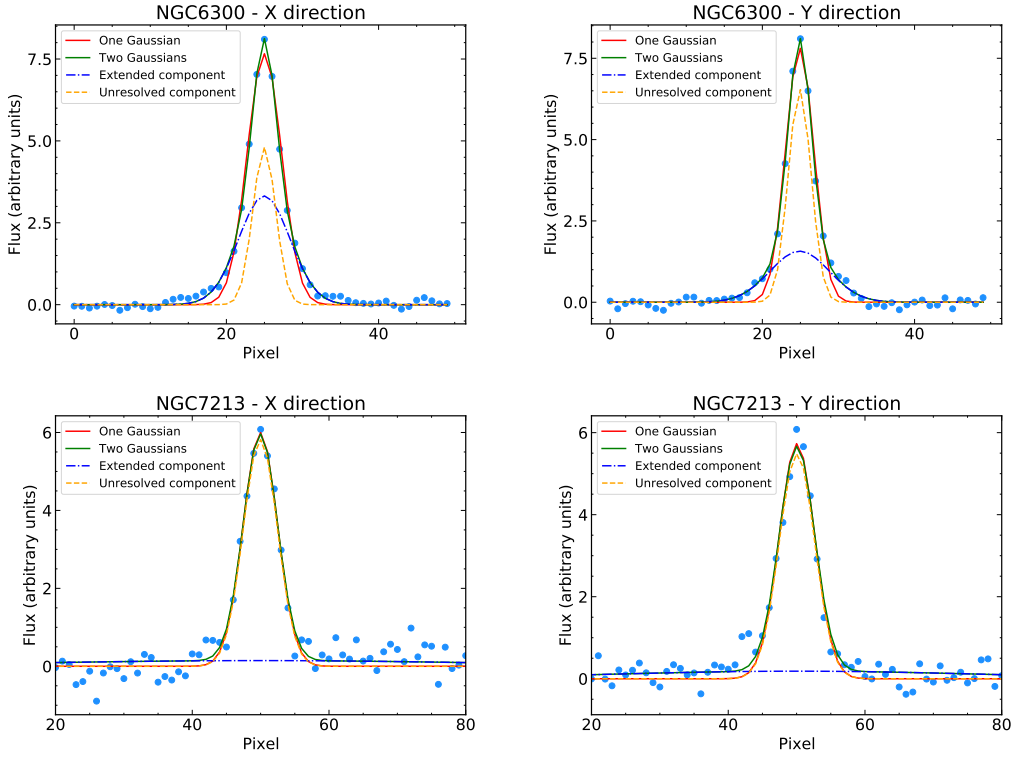

Fig. 1. Examples of the fits of the 1D mid-IR profiles extracted along the *X* and *Y* directions for two galaxies in our sample. The *top panels* are for NGC 6300, which is a case with a large fraction of extended mid-IR emission, whereas the *bottom panels* are for NGC 7213, which appears unresolved at the angular resolution of the mid-IR observations. The cyan dots are the observations and the red lines are the result of fitting the galaxy profile with just one Gaussian function. The green lines are the result of fitting the galaxy profile with the sum of two Gaussian functions, one to represent the unresolved component (orange dashed lines) and the second the extended emission (blue dotted-dashed lines).

emission and are large enough to include the PSF wings. For the five galaxies with faint or no detected extended mid-IR emission, the unresolved emission contributes between 80 and 100%, within similar apertures. This is in good agreement with previous works (Asmus et al. 2014; García-Bernete et al. 2016; Asmus 2019). In summary, at our angular resolutions the unresolved component accounts for between 60 and 100% of the mid-IR emission in the central 1.5″ ∼ 150 pc for the majority of the galaxies in our sample.

3.3. Comparison with ALMA 870 μm and CO(3–2) observations

To compare the mid- and far-IR morphologies, we first adjusted the astrometry of the mid-IR images of the seven galaxies with extended emission. We assumed that the peak of the mid-IR emission coincides with that of the ALMA 870 μm continuum emission and adjusted the mid-IR coordinates accordingly. Figure 3 (left panels for each galaxy) shows in color the original ALMA continuum images, that is, including both the unresolved and the extended emission, with the contours showing the extended mid-IR emission from the PSF-subtracted images. In the six out of the seven galaxies with extended mid-IR emission, GB21 concluded that the ALMA 870 μm extended emission traces cold dust mostly along the equatorial material in the torus, with sizes between 28 and 129 pc (median of 42 pc, Table 3).

In NGC 1365, NGC 3227, and NGC 7582 as well as the inner regions of NGC 5506, the extended mid-IR emission appears to be approximately perpendicular (in projection) to the extended ALMA 870 μm continuum emission. The latter for these four galaxies is identified as the torus. In NGC 5643, the orientation of the extended mid-IR emission is mostly along PA_{MIR} = 60−70°, which is nearly perpendicular (in projection) to the nearly north-south ALMA 870 μm continuum emission. Finally, in NGC 6300 the extended mid- and far-IR emission show similar orientations, and thus the extended mid-IR emission is along the equatorial direction of the torus.

GB21 showed that the nuclear CO(3−2) morphologies of the GATOS Seyferts are in most cases rather different from the 870 μm emission. We constructed red-green-blue (RGB) images using the ALMA CO(3−2) images in red and 870 μm continuum in green for the seven Seyferts with extended mid-IR emission. In blue we show only the extended mid-IR emission to emphasize the low surface brightness emission at these wavelengths. In all galaxies but NGC 6300 (see right panels of Fig. 3), the extended mid-IR emission appears to fill the nuclear regions where the CO(3−2) emission is fainter. On larger scales the CO(3−2) emission is more extended than both the mid- and far-IR continuum images. In NGC 5643 the extended mid-IR emission is not only along the east-west direction, where there is faint CO(3−2) emission, but also along the nuclear molecular gas minispiral.

3.4. Comparison with ionization cones, NLR, and nuclear outflows

The seven galaxies with extended mid-IR emission have bright ionization cones/NLR that are identified from optical and near-IR narrow-band imaging and/or integral field unit (IFU) spectroscopy. We derived the PA of the cones by visual inspection of the [O III]λ5007 images from Venturi et al. (2018) for

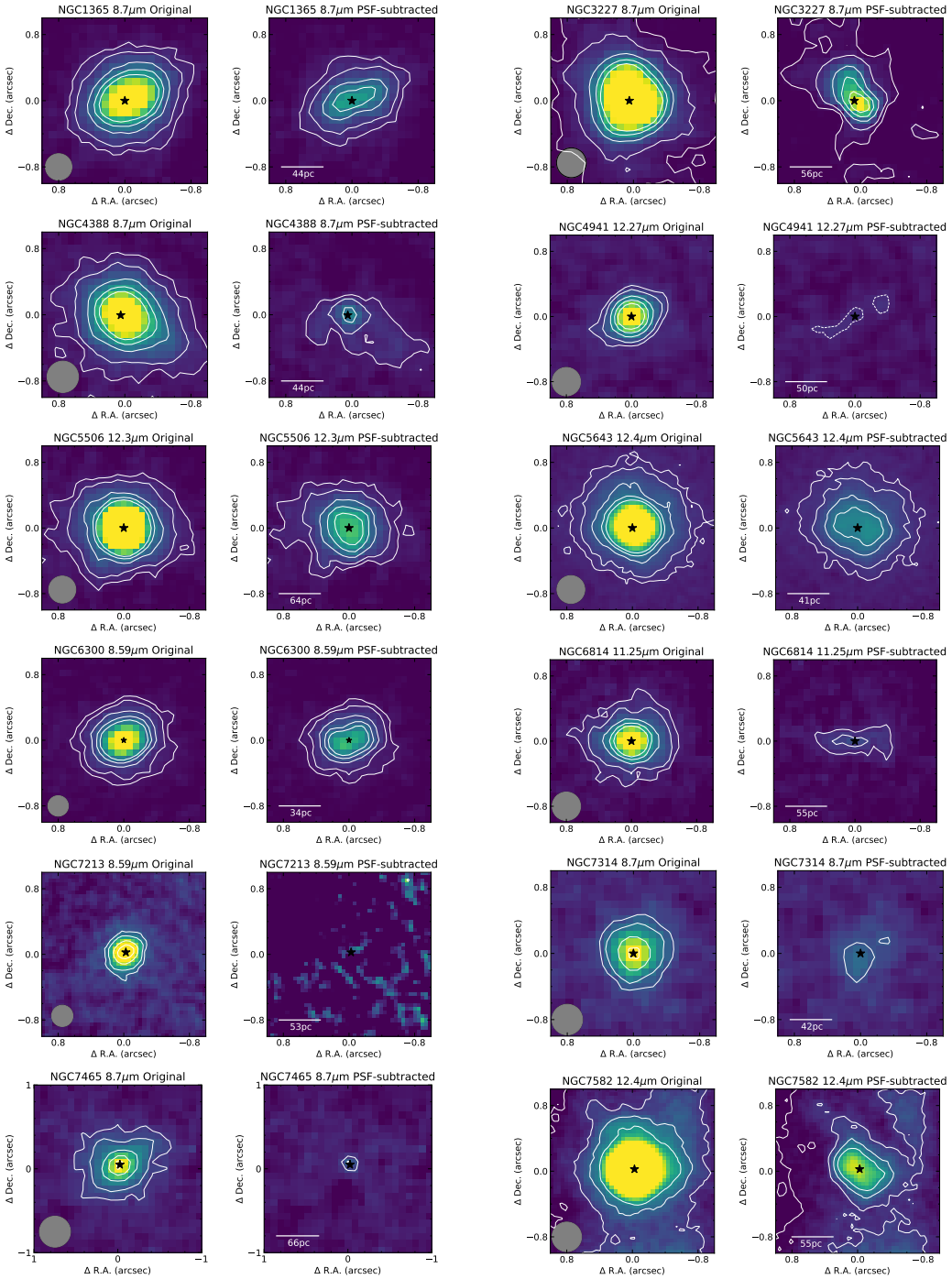

Fig. 2. Mid-IR images of the central 2″ × 2″. For each galaxy, the *left* and *right panels* are the original and the PSF-subtracted images, respectively. The gray circles indicate the FWHM of the standard star as fit with a 2D Gaussian. The star symbol marks the peak of the mid-IR emission before PSF subtraction. The first contour with a solid line is at a $3 \times \sigma_{bk}$ level and the next contours are at 5, 10, 15, $20 \times \sigma_{bk}$ levels. For NGC 4941 the dashed lines in the PSF-subtracted image are $2 \times \sigma_{bk}$. All the images are oriented north up, east to the left. We smoothed the original and PSF-subtracted images with a Gaussian function (see text for more details). For each galaxy we display the two images with the same intensity and contour levels.

NGC 1365, from Schmitt et al. (2003) for NGC 4388, from Fischer et al. (2013) for NGC 5506, from García-Bernete et al. (2021) for NGC 5643, and from Thomas et al. (2017) for NGC 7582. For NGC 3227 we used *Hubble* Space Telescope (HST) narrow-band images from Alonso-Herrero et al. (2019). For NGC 6300, Davies et al. (2014) detected a nuclear molecular gas outflow using observations of the H_2 2.12 μm line. We list the values of PA_{cone} in Table 3 and plot them in Fig. 3. All seven galaxies have large projected opening angles of the cones/outflows, ranging from 85 to 115°, approximately.

Six of the seven GATOS Seyferts with extended mid-IR emission show nearly the same orientations for the extended mid-IR emission and the ionization cones/outflows (Fig. 3, left panels). The exception is NGC 6300 (see below). The differences in (projected) orientations for these six Seyferts are less than 10−20°. These are in good agreement with the typical values

Table 3. Observational and modelled torus and wind properties.

	Torus or disk							Wind		
	ALMA		i_{torus} (°)					i_{cone} (°)	PA_{cone} (°)	f_{wd}
Galaxy	d (pc)	PA_A (°)	CLUMPY	CAT3D-WIND	XCLUMPY	ALMA	Kinem.	Model	Opt/IR	CAT3D-WIND
NGC 1365	28	50	[8–40]	...	53	>48	...	...	−45	...
NGC 3227	41	166	[9–35]	[28–32]	20 (f)	>50	30	75	35	>0.5
NGC 4388	32	−43 (*)	[13–20]	[50–52]	70	...		...	−165	>0.7
NGC 4941	78	−29 (*)	...	[35–41]	...	...	...	...	40	[0.2–0.3]
NGC 5506	129	87	[5–40]	Low	33	>55		10	18	>0.7
NGC 5643	43	4	[65–81]	...	74 (f)	>39	60	25	82	...
NGC 6300	64	85	[14–21]	Low	53	>44	57	...	18	[0.2–0.3]
NGC 6814	33	57 (*)	[7–34]	30	45 (f)	...	...	...	33	[0.2–0.3]
NGC 7213	40	71	[0–30]	Low	45 (f)	>30	...	...	No	<0.2
NGC 7314	60	21	[5–37]	High	45 (f)	>58	...	...	110	>0.7
NGC 7465	67	4	...	...	...	>53	...	...	−72	...
NGC 7582	91	−18	[53–82]	...	41	>59	59	...	−122	...

Notes. Columns for the torus or disk components are as follows. d is the ALMA MSR 870 μm torus size (diameter of the extended component at the 3σ level) and PA_A the position angle PA and inclination, from GB21. (*)The 870 μm PA is not along the equatorial direction (i.e., torus). The torus or disk inclination (i_{torus}) constraints from modeling of the IR emission with the CLUMPY torus models are from Alonso-Herrero et al. (2011, 2012), Ruschel-Dutra et al. (2014), Ichikawa et al. (2015), García-Bernete et al. (2019), Martínez-Paredes et al. (2020), the CAT3D-WIND models from González-Martín et al. (2019), and from modeling of X-ray observations are from Walton et al. (2010), Tanimoto et al. (2020), Ogawa et al. (2021). The torus inclinations from the ALMA MSR 870 μm images are from GB21 and from the ALMA CO(3−2) and CO(2−1) kinematics are from Alonso-Herrero et al. (2018, 2019) and GB21. Columns for the wind components are as follows. The ionization cone inclination (i_{cone}) constraints are from the modeling of the NLR by Fischer et al. (2013). PA_{cone} is the position angle of the ionization cones and the references are given in the text in Sect. 3.4. The wind-to-disk ratio f_{wd} constraints are from modeling with the CAT3D-WIND models from González-Martín et al. (2019).

found by Asmus et al. (2016), Asmus (2019) for a larger sample of nearby AGN with prominent extended mid-IR emission. The extended mid-IR emission in NGC 3227, NGC 4388, and NGC 7582 is more prominent on the optical bright side of the ionization cone. In NGC 1365, NGC 5506, and NGC 5643 the mid-IR extended emission is more symmetric around the AGN position and approximately along the direction of the ionization cone. In the innermost region of NGC 5643, the extended mid-IR emission is at $PA_{MIR} \sim 48°$, which could be due to emission in the northeast inner walls of the ionization cone (see Fig. 22 of Fischer et al. 2013), becoming progressively more aligned with the ionization cone in the outer regions. In the inner regions of NGC 5506, $PA_{MIR} \sim 30°$, which is nearly aligned with the orientation of the cone, whereas at larger radial distances the extended mid-IR emission becomes more equatorial.

The extended mid-IR emission of NGC 6300 appears to be perpendicular to the orientation of the ionization cone. The morphology and orientation of the mid-IR extended emission are, on the other hand, similar to that seen in the HST $V-H$ color map (Martini et al. 2003; Davies et al. 2014), which likely traces dust in the host galaxy. The outer regions of NGC 5506 also show a large difference between the projected orientations of the cones and mid-IR extended emission. This indicates that the extended mid-IR emission along the approximate east-west direction also traces dust emission in the highly inclined host galaxy, as seen again from the $V-H$ color map (Martini et al. 2003). In NGC 7582, the extended mid-IR emission additionally probes dust in regions in the circumnuclear ring of star formation (Wold & Galliano 2006).

NGC 4941, NGC 7465, and NGC 7314 have extended optical NLRs, which are detected with optical IFU observations and/or HST imaging (see Erroz-Ferrer et al. 2019; Ferruit et al. 2000; Sousa et al., in prep., respectively). In NGC 6814, the NLR and the coronal line region are rather compact and there is evidence for ionized outflows on these scales (∼1″, see Müller-Sánchez et al. 2011). In these four galaxies we do not detect extended mid-IR emission.

4. Dependence of warm dust morphologies on the Eddington ratio and nuclear column density

In the previous section, we showed that there is extended mid-IR emission approximately along the polar direction in six out of the 12 GATOS Seyferts analyzed in this work. It is yet unknown whether this polar dust emission is simply due to dust near the edges of the NLR being illuminated by the AGN, part of a nuclear dusty outflow or both. On the other hand, another four galaxies in our sample show NLR emission but no evidence for bright extended mid-IR emission. In this section we investigate if the nuclear column densities and Eddington ratios in the galaxies in our sample are likely to launch dusty outflows.

The gas and dust in the immediate surroundings of an active nucleus are subject to the AGN radiation pressure. The idea of infrared radiation pressure was first put forward by Pier & Krolik (1992b) and developed further by Krolik (2007), as an explanation to support the vertical height of the torus. In the classical Eddington limit, only the electron scattering is taken into account. Because the opacity of the dust is much greater than the Thomson opacity, there is an effective Eddington ratio, which Krolik (2007) estimated to be of the order of 10% the classical Eddington ratio. In other words, in the presence of dust, the effects of the radiation pressure are boosted. Thus, at high Eddington ratios, although not necessarily $\lambda_{Edd} \geq 1$, and moderate column densities, nuclear outflows may be present (see Fabian et al. 2008, and references therein). These outflows

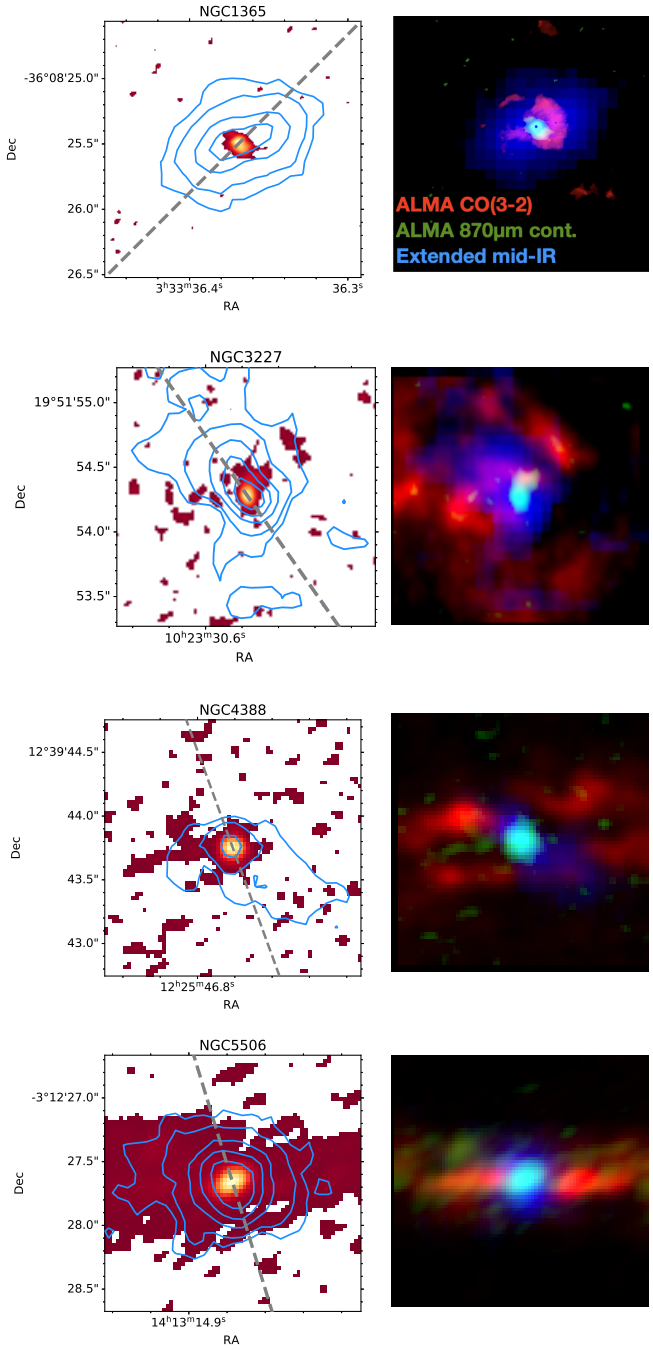

Fig. 3. Galaxies with extended mid-IR emission. *Left panels*: in color are the ALMA MSR 870 μm continuum images (with both the unresolved and the extended emission) from GB21. The blue contours are the mid-IR PSF-subtracted images with the same levels as in Fig. 2. The FoV is 2″×2″. We also plot with the dashed lines the approximate PA of the ionization cones, NLR and/or outflows (see Sect. 3.4). *Right panels*: RGB images constructed with the ALMA CO(3−2) image (red), ALMA 870 μm continuum (green), and extended mid-IR emission (blue). The FoV is approximately the same as in the left panels.

might even clear out the gas from the nuclear region (see also Ricci et al. 2017b).

Venanzi et al. (2020) demonstrated semi-analytically that IR-dominated winds can be launched more efficiently when the acceleration due to the AGN radiation pressure ($a_{\rm AGN}$) and the acceleration due to the gravitational force ($a_{\rm g}$) from the central black hole are balanced (see also Tazaki & Ichikawa 2020).

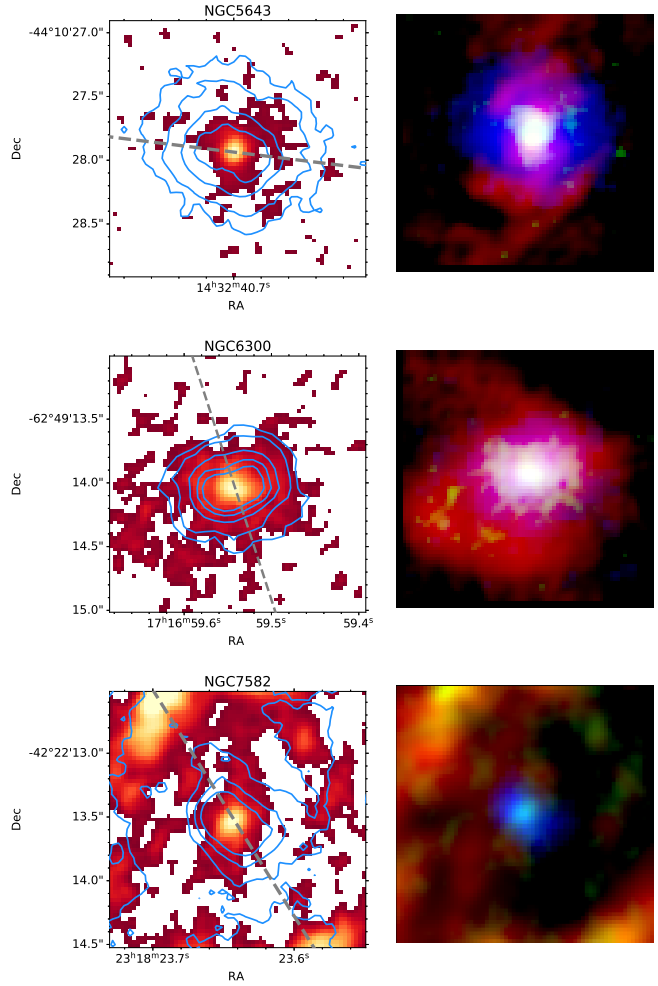

Fig. 3. continued.

Their radiation dynamical simulations for the typical Eddington ratios of Seyfert galaxies showed that IR-dominated outflows would take place at moderate column densities of a few $N_{\rm H} \sim 10^{23}$ cm^{-2}. At higher column densities of approximately $N_{\rm H} \geq 10^{24}$ cm^{-2}, they predicted that the lifting of the dusty clumps is suppressed and this material settles in the disk plane.

In Fig. 4 we show the hydrogen column densities or upper limits derived toward the AGN position of the GATOS Seyferts against the Eddington ratios. We used the ALMA estimates of $N_{\rm H2}$ from GB21 (see also Table 1), which were derived using the CO(3−2) data and the canonical CO-to-H_2 conversion factor of the Milky Way. The ALMA $N_{\rm H2}$ values correspond to physical resolutions of 7−10 pc. To derive $N_{\rm H}$, we assumed that the molecular gas phase is dominant on these scales (see for instance the simulations of Wada et al. 2016). We note that these values are not the measured column densities of the individual clumps. However, they likely give an estimate of the average properties of the clumps modulo the (unknown) filling factor. In X-rays, the derived $N_{\rm H}$ are only along the line of sight. We therefore assume that $N_{\rm H}$ (ALMA) for each galaxy is representative of those clouds located in the dusty wind launching region. We also included in this figure NGC 1068 and Circinus, which show clear polar mid-IR emission (see Cameron et al. 1993; Packham et al. 2005a, respectively). For the latter, the ALMA hydrogen column densities are from García-Burillo et al. (2019) and Izumi et al. (2018), respectively.

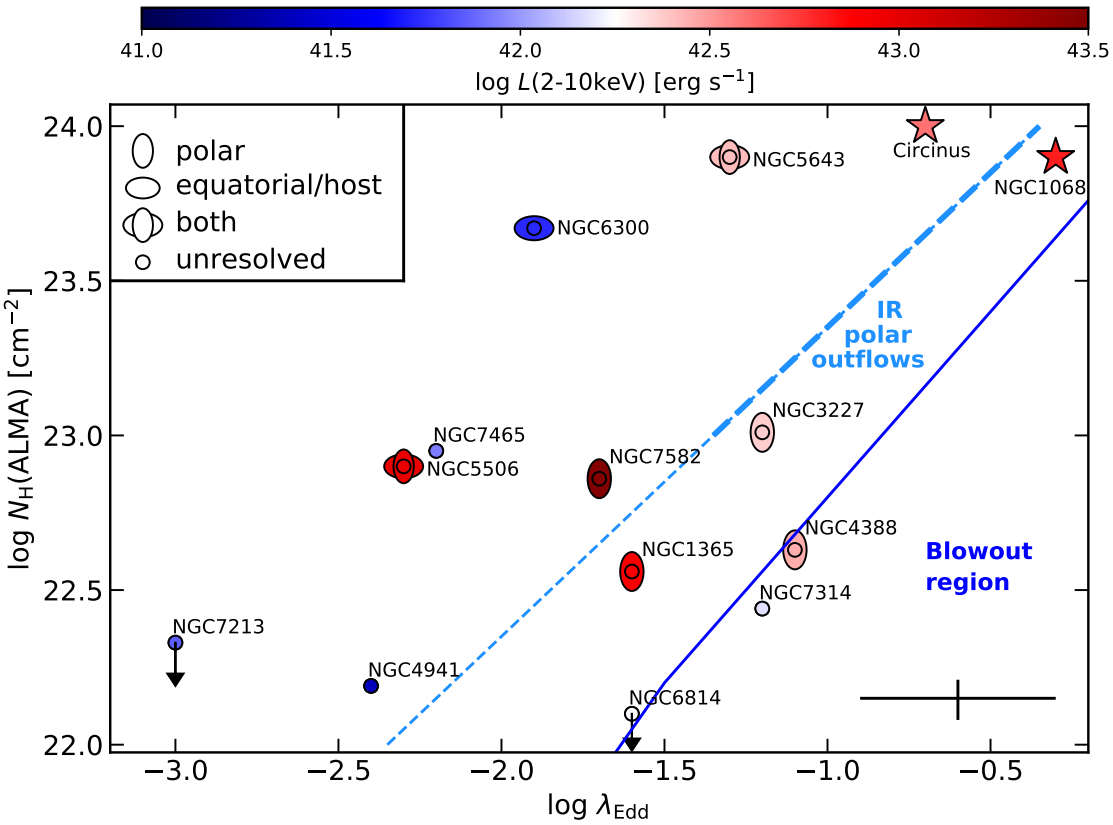

Fig. 4. Diagram showing the nuclear hydrogen column densities against the Eddington ratios for the GATOS Seyferts. The hydrogen column densities are from ALMA CO(3−2) based H_2 estimates at the AGN position from GB21. The symbols are color-coded in terms of the intrinsic 2−10 keV luminosities. The different symbols indicate the mid-IR morphologies (see Table 2). Circinus and NGC 1068, which are marked with star symbols, also show polar mid-IR emission but are not included in our sample. The error bars represent typical uncertainties in the observations, namely, 0.3 dex for the Eddington ratios and a 15% uncertainty in the absolute flux calibration of the ALMA data. Below the solid curve from Fabian et al. (2008) is the blowout region where outflows are likely to clear material in the nuclear regions (see also Ricci et al. 2017b). The dashed line from Venanzi et al. (2020) indicates the limit where the AGN radiation acceleration balances gravity and the IR radiation pressure dominates giving rise to polar dusty outflows. Their radiation-dynamical simulations were for a column density range $N_H \simeq 10^{23}$−10^{24} cm^{-2}, which we mark with the thicker dashed line.

We also plot in this figure the predicted blowout region (the area below the solid line) derived by Fabian et al. (2008), which is not populated by AGN. The area in this figure near the dashed line (computed when $a_{AGN}/a_g \equiv 1$, see Venanzi et al. 2020), shows the region where we would expect to find AGN with IR-dominated outflows. As discussed by these authors, below approximately $N_H = 10^{22}$ cm^{-2} which is equivalent to an optical depth in the near-IR below one, the driving of infrared radiation is not effective.

We find that the GATOS Seyferts with extended mid-IR emission in the (projected) polar direction (NGC 1365, NGC 3227, NGC 4388, and NGC 7582) as well as NGC 1068 and Circinus are located close to the region where polar dusty outflows are more likely to be launched. Among these galaxies, NGC 3227 and NGC 1068 present evidence of molecular outflows in CO transitions on the torus scales (~20−40 pc, see Alonso-Herrero et al. 2019; García-Burillo et al. 2019). The ALMA observations of Circinus show, on the other hand, a nuclear outflow with a modest velocity (Izumi et al. 2018). These authors predicted that a significant mass in the wind will fall back to the disk. NGC 3227, NGC 4388, and NGC 7582 as well as NGC 1068 show evidence of molecular outflows on physical scales larger than the torus (up to a few hundred parsecs, see Davies et al. 2014; García-Burillo et al. 2019; Domínguez-Fernández et al. 2020, and GB21), which are more likely due to the interaction between the AGN wind and/or a radio jet if present and molecular gas in the disk of the host galaxy.

NGC 5643 and NGC 5506 appear to have extended both polar and equatorial mid-IR emission. In NGC 6300 the mid-IR emission might be due to dust in the equatorial direction of the torus as well as in the host galaxy. According to the Venanzi et al. (2020) simulations, galaxies with relative high Eddington ratios that lie to the left of the dashed line might be more conducive to having equatorial outflows. This is the case for NGC 5643 (see Alonso-Herrero et al. 2018). Moreover, these equatorial outflows are not likely to be efficient (maybe not just yet) at clearing the nuclear regions of NGC 5643 and NGC 6300 (and others), as shown observationally by GB21.

NGC 6814 and NGC 7314 are close to the blowout region, where polar dusty outflows should not be prominent. The CO(3−2) map of NGC 6814 of GB21 (their Fig. 10) shows that there is little molecular gas in the nuclear and circumnuclear regions of this galaxy, in agreement with being in the blowout region and an unresolved mid-IR morphology. NGC 7314, on the other hand, contains more molecular gas with two CO peaks located symmetrically around the AGN in the inner 40 pc (Fig. 13 of GB21). This might indicate that some clearing of molecular gas at the AGN location already took place in the nuclear regions of this galaxy. For this galaxy, the mid-IR

emission is mostly unresolved. Finally the low nuclear column density and Eddington ratio of NGC 4941 and NGC 7213 place these galaxies in a region in Fig. 4 where dusty winds are not launched. This is in agreement with the unresolved mid-IR morphology.

In summary, seven galaxies in our sample show both Eddington ratios and nuclear column densities favorable to launching polar and equatorial dusty winds. The remaining have either low nuclear hydrogen column densities and/or low Eddington ratios, and thus dusty winds might not be likely.

5. CAT3D-WIND mid- and far-IR model images

In Sect. 3.3 we showed that there is a diversity of nuclear (1−1.5″) mid-IR morphologies in the GATOS Seyferts with the unresolved component dominating the emission. At 870 μm, on the other hand, GB21 found that the extended component is dominant on these scales.

In this section we use the radiative transfer model of a clumpy disk and wind dubbed CAT3D-WIND and presented in Hönig & Kishimoto (2017) to generate model images in the mid- and far-IR. The goal is to explore the morphologies at these wavelengths for several disk and wind configurations and geometries as informed by fits to their IR emission. In Sect. 6 we then simulate CAT3D-WIND model images with angular resolutions corresponding to those of our mid-IR and ALMA observations.

5.1. Brief description of the models

The CAT3D-WIND model includes both a traditional dusty clumpy disk (or geometrically thin torus), which is based on that of Hönig & Kishimoto (2010), and a dusty clumpy wind perpendicular to the torus. The latter is included to account for the polar dust emission detected in local AGN (see, e.g., Asmus et al. 2016; Asmus 2019). The clouds have an optical depth of $\tau_V = 50$ and N_0 describes the number of clouds along the equatorial direction of the torus. The clouds are distributed following a radial power law ($\propto r^a$) with indices a for the disk and a_w for the wind. The wind-to-disk ratio f_{wd} is the number of clouds along the cone with respect to N_0. The vertical distribution of the disk follows a Gaussian distribution $\propto \exp^{-z^2/(2(hr)^2)}$ with a dimensionless scale height h and the vertical distance from the mid-plane z in units of the sublimation radius (r_{sub}). The wind is modelled as a hollow cone with a half-opening angle of θ_w and walls with an angular width of σ_θ. Figure 5 shows a sketch of the model and its parameters.

The inner radius is determined by the dust r_{sub}, which the model takes as $r_{mod} = 0.3$ pc at $L_{bol} = 10^{46}$ erg s^{-1} and the scaling is then $r_{sub} = r_{mod} \times (L_{bol}/10^{46}\,\mathrm{erg\,s^{-1}})^{1/2}$ (see Hönig & Kishimoto 2010, for more details). L_{bol} is the accretion disk bolometric luminosity computed as $L_{bol} = 8 \times \nu L_\nu(V)$.

5.2. Selection of model parameters and generation of model images

The CAT3D-WIND model has a large number of parameters to describe the disk and the wind components (see Table 1 of Hönig & Kishimoto 2017). Since we are interested in comparing the observed mid- and far-IR observations of the GATOS Seyferts with CAT3D-WIND model images, in this work we concentrate on some of the main parameters that define the geometry and thus are more likely to control the morphologies. These are the indices of the radial distribution of the clouds in the disk and the wind (a and a_w), the wind-to-disk ratio of clouds (f_{wd}), as well as the inclination. As we shall see, the disk height and angular width of the cone walls play an important role on the self-obscuration of the disk and wind in the mid-IR.

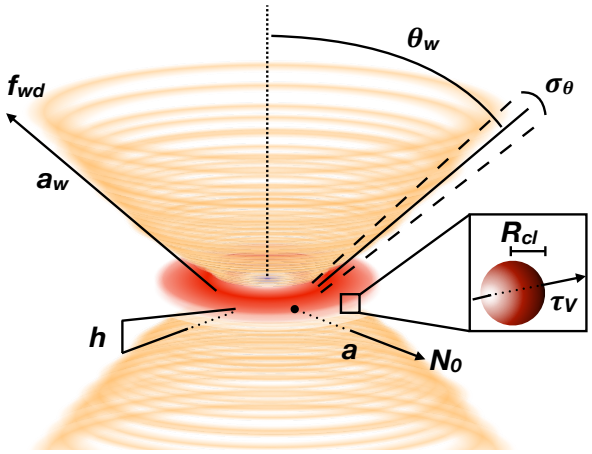

Fig. 5. Cartoon showing the CAT3D-WIND geometry. In red is the clumpy disk component and in orange the dusty clumpy wind, which is represented as a hollow cone. The model parameters are also marked (see Sect. 5.1 and Table 4).

González-Martín et al. (2019) fit *Spitzer*/IRS spectroscopy of a large sample of local AGN using a variety of torus models, including CAT3D-WIND. They found that CAT3D-WIND provided a good fit for approximately half of their sample. In particular, they reproduced better the mid-IR spectra of type 1 AGN than type 2 as well as the spectra of the more luminous AGN in their sample. Eight of the GATOS Seyferts are in their sample. Rather than focusing on the individual fits, we based our choice of the CAT3D-WIND parameters on the derived ranges (see Table 4 and below) for these Seyferts, regardless of whether we detected a bright extended mid-IR component or not. We included the following combinations of cloud radial distributions:

- compact disk – extended wind, $a = -2$ and $a_w = -0.5$
- extended disk – compact wind, $a = -0.5$ and $a_w = -2$
- compact disk – compact wind, $a = -2$ and $a_w = -2$
- extended disk – extended wind, $a = -0.5$ and $a_w = -0.5$.

We used four values of the wind-to-disk ratio of clouds: $f_{wd} = 0.3, 0.6, 0.9, 1.2$ and four values of the inclination: $i = 30°$ (nearly face-on view of the disk), 45, 60, and 75° (nearly edge-on view of the disk). We fixed the following parameters, $N_0 = 10$ and the half-opening angle of the wind $\theta_w = 45°$. We took ranges of the angular width of the wind $\sigma_\theta = 5, 10, 15°$ and height of the disk $h = 0.1, 0.2, 0.3$. We distributed the dust over a region of $2000\,r_{sub} \times 2000\,r_{sub}$ in size. This corresponds to typical physical sizes of tens of parsecs for our sample (see Sect. 6.2), which are needed to reproduce the relatively large ALMA tori.

We additionally generated CAT3D-WIND model images for the specific cases of NGC 7213 and NGC 6814, for which González-Martín et al. (2019) derived some model parameters outside the range found for the rest of the galaxies in our sample. In particular, they fit relatively low values of the number of clouds along the disk equator, the fraction of wind-to-disk cloud ratio, and inclination. The low N_0 fit agree with the relatively little amounts of nuclear cold molecular gas (see Alonso-Herrero et al. 2020, and GB21, see also Table 1) detected in these two galaxies. Table 4 summarizes the

Table 4. CAT3D-WIND model parameters used in this work.

Name	Symbol	Range	NGC 7213, NGC 6814
Disk radial index	a	[−0.5, −2]	−1
Wind radial index	a_w	[−0.5, −2]	−0.5
Wind-to-disk cloud ratio	f_{wd}	[0.3, 0.6, 0.9, 1.2]	0.15
Number of clouds along disk equator	N_0	10	5
Inclination (°)	i	[30, 45, 60, 75]	[0, 15, 30]
Disk height	h	[0.1, 0.2, 0.3]	0.1
Wind angular width (°)	σ_θ	[5, 10, 15]	10

Notes. The common parameters are a cone opening angle of $\theta_w = 45°$ and the optical depth of the clouds $\tau_v = 50$.

CAT3D-WIND parameters selected to generate model images in this work.

We generated model monochromatic images at two mid-IR wavelengths, namely, $\lambda = 8$ and $\lambda = 12\,\mu$m to approximately encompass those of the central wavelengths of the observation filters. We used as a far-IR wavelength $\lambda = 700\,\mu$m, which is one of the wavelengths of the model standard grid (the next one is 1000 μm). Taking into account the model parameters (see Table 4) and the three wavelengths, we generated a total of $1728 + 9$ model images[3]. We resampled the images from the model natural resolution of $2\,r_{sub}$ to a pixel size of $10\,r_{sub}$. As we shall see in Sect. 6.2, this resolution is higher than that achieved with the current ground-based mid-IR imaging and ALMA angular resolutions. We also note that the 8 and 12 μm model images are similar and thus, we only show in the figures an discuss in the following sections the former.

5.3. "Thin" geometries

We start by presenting the model images for a "thin" geometry, that is, a disk height $h = 0.1$ and cone walls with $\sigma_\theta = 5°$. This geometry suffers less from self-obscuration effects. Figures 6 and 7 show the mid- and far-IR images for the compact disk-extended wind and extended disk – compact wind combinations, at the four selected inclinations and for an intermediate value of the wind-to-disk ratio, $f_{wd} = 0.6$ (see appendix for images with $f_{wd} = 1.2$). In Figs. A.1 and A.2 we show the compact disk – compact wind and extended wind – extended disk configurations. In all the figures, we plotted the images in a linear scale and with the same scaling values for all geometries and inclinations.

The wind component is clearly observed at intermediate-to-high inclinations and is more prominent, as expected, when the wind is in an extended configuration (Figs. 6 and A.2). Moreover, the characteristic "X"-shape of the wind is most notable in the far-IR. At this wavelength the dust is optically thin. The disk and wind can have comparable far-IR brightnesses in the compact disk – extended wind configuration at relatively high inclinations ($i = 60°$ and 75°, two bottom panels of Fig. 6). The disk component, on the other hand, is brighter than the wind in the far-IR for the compact wind configurations (see Figs. 7 and A.1). In the extended disk configurations (Figs. 7 and A.2), the far-IR emission of the disk shows a ring-like morphology at all inclinations whereas in the compact disk configurations (Figs. 6 and A.1) the far-IR emission peaks at the central position.

[3] The CAT3D-WIND model images and corresponding SEDs can be found at http://cat3d.sungrazer.org

In the mid-IR, two-sided polar wind emission is also present at $i = 45°$ for the compact disk and extended wind configuration (see second panel from the top in Fig. 6). However, even for this "thin" geometry, it suffers moderately from self-obscuration due to the cone walls. Clearer two-sided polar morphologies in the mid-IR are seen in other geometries with the CAT3D-WIND models (see Fig. 1 of Hönig & Kishimoto 2017) and other models (see for instance, Schartmann et al. 2014; Gallagher et al. 2015; Stalevski et al. 2017). We note that even at $i = 75°$ the disk component is quite prominent in the mid-IR in our "thin" geometry. For the wind-to-disk ratio considered in this section ($f_{wd} = 0.6$) and the majority of the disk-wind configurations and inclinations, the mid-IR emission comes mostly from the inner part of the disk and cone. For higher values of f_{wd}, biconical and one-sided polar emission morphologies in the mid-IR become more apparent (see Figs. A.5 and A.8). At lower inclinations, part of the mid-IR emission arises from the far side of the cone at radial distances close to the heating source. It is also possible to observe both bright mid- and far-IR emission along the equatorial direction of the disk in the extended disk – compact wind configuration at high inclination (see the bottom panels of Fig. 7).

5.4. "Thick" geometries

Figures 8, 9, A.3, and A.4 present the images for "thick" geometries, that is, a disk height of $h = 0.3$ and cone walls with $\sigma_\theta = 15°$, and $f_{wd} = 0.6$. We note that this "thick" geometry does not mean a geometrically thick torus. None of the generated model images produces clear biconical dust emission morphologies in the mid-IR and at high inclinations ($i = 75°$). Our value of $\sigma_\theta = 15°$ produces relatively thick cone edges that obscure the near side of the cone. A similar effect also takes place for large values of f_{wd} when the number of clouds in the cone line-of-sight becomes too large.

At low and intermediate inclinations ($i = 30, 45°$), there is one-sided polar dust emission in the mid-IR in all geometries (Figs. 8, 9, and A.4) except for the compact disk – wind configuration. This mid-IR polar dust emission is only seen projected on the far side of the disk and is due to self-obscuration of the near side of the cone and disk. This morphology appears in all the values of the wind-to-disk ratio explored in this work. Torus models without the wind component can also produce this one-sided polar emission at intermediate inclinations and relatively large torus angular widths (see, e.g., Schartmann et al. 2008; Siebenmorgen et al. 2015; Lopez-Rodriguez et al. 2018; Nikutta et al. 2021). The details of the mid-IR morphology in the model images also depend on how obscuring the cone edges are (that is, the thickness of the cone walls).

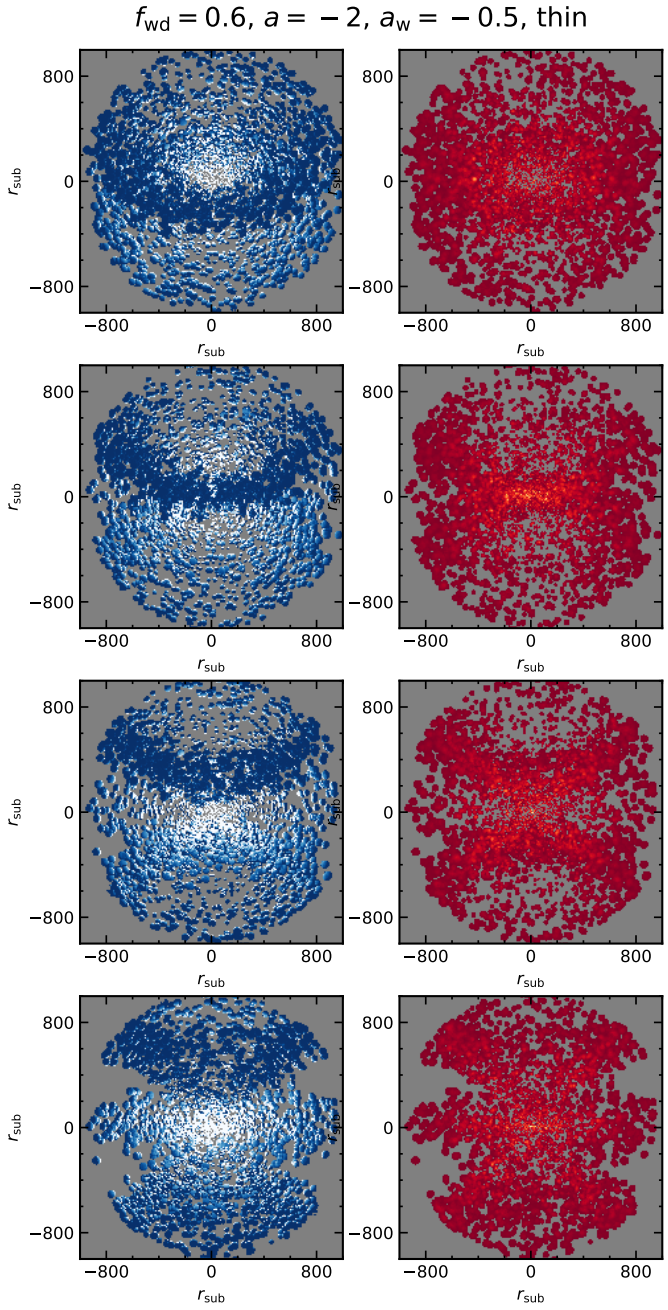

Fig. 6. CAT3D-WIND model images with a "thin" ($h = 0.1$ and $\sigma_\theta = 5°$) geometry and $f_{wd} = 0.6$. We show the 8 μm (in blue colors, *left panels*) and 700 μm (in orange colors, *right panels*) emission for a compact disk ($a = -2$) and an extended wind ($a_w = -0.5$). The resolution of the model images is 10 r_{sub} per pixel. *From top to bottom*: the inclinations are $i = 30°$ (nearly face-on disk), 45°, 60°, and 75° (nearly edge-on disk). We list the rest of parameters in Table 4. The color scales are such that dark blue and dark orange indicate fainter emission, white/yellow is brighter emission, and gray means no emission.

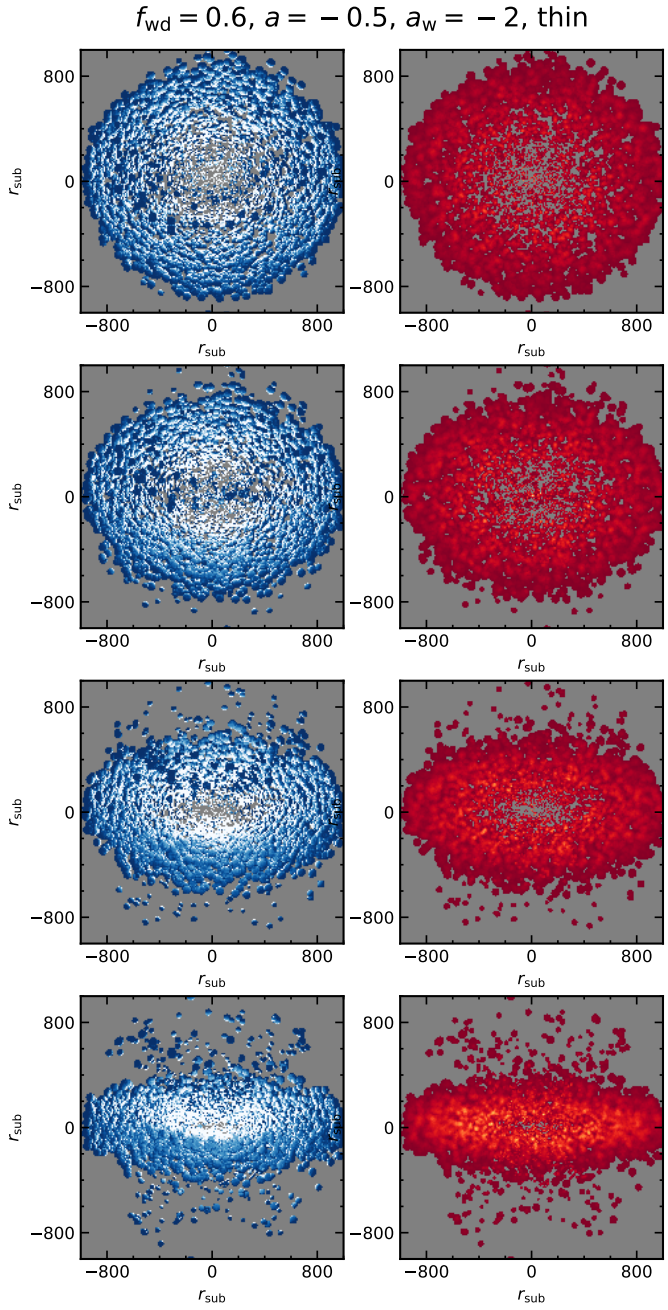

Fig. 7. CAT3D-WIND model images for a "thin" geometry and $f_{wd} = 0.6$ at 8 μm (in blue colors, *left panels*) and 700 μm (in orange colors, *right panels*) for an extended disk ($a = -0.5$) and a compact wind ($a_w = -2$). *From top to bottom*: the inclinations are 30° (nearly face-on disk), 45°, 60°, and 75° (nearly edge-on disk).

In the two extended disk configurations (Figs. 9 and A.4), the mid- and far-IR emissions have complementary morphologies. At low and intermediate inclinations ($i = 30–60°$), most of the mid-IR emission comes from the inner regions of the disk and the edges of the cone, whereas the far-IR emission is produced in the outer regions with an apparent ring-like morphology. At high inclinations, most of the far-IR emission comes from the disk that shows a puffed-up morphology due not only to the thicker disk but also to the additional contribution from cold dust in the wind.

There is also polar dust emission in the far-IR with the characteristic "X"-shape at $i = 60$ and $i = 75°$ for the extended wind configurations (Figs. 8 and A.4). The constrast of the "X"-shape is however lower than in the "thin" geometry. Nevertheless, in the model with the steep cloud distribution profile in the disk (compact disk), this shape is seen more clearly. This is because in this configuration there are not too many clouds left at larger distances, so relatively more far-IR emission is coming from the cone edges.

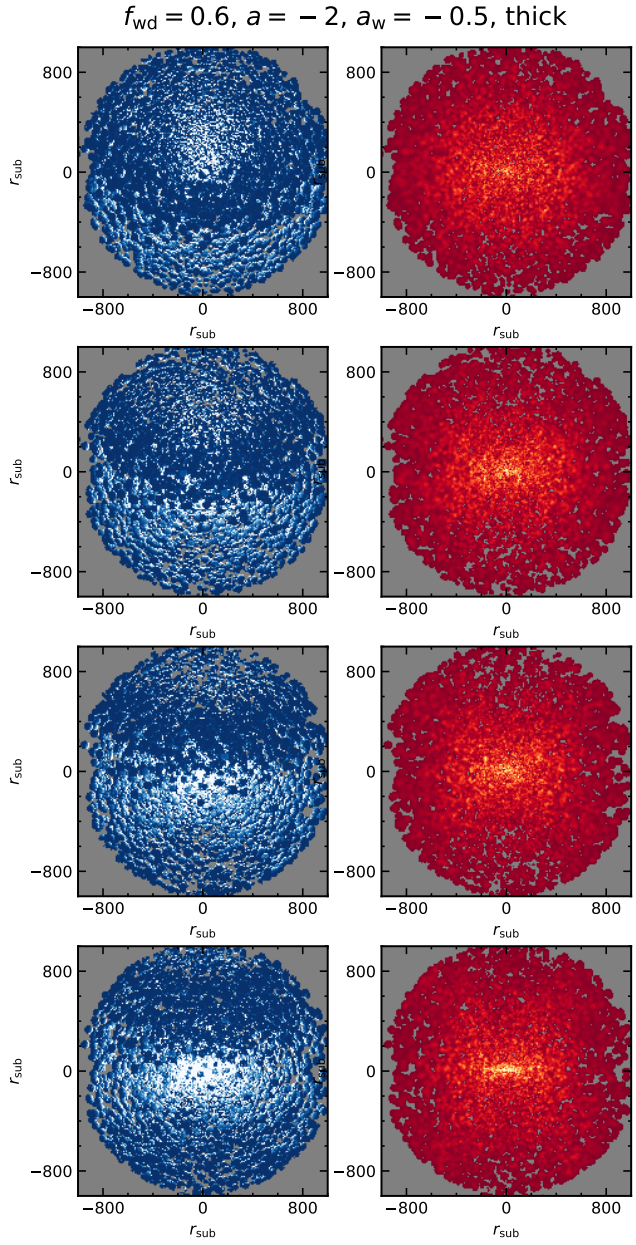

Fig. 8. CAT3D-WIND model images with a "thick" geometry ($h = 0.3$ and $\sigma_\theta = 15°$) and $f_{wd} = 0.6$. We show the 8 µm (in blue colors, *left panels*) and 700 µm emission (in orange colors, *right panels*) for a compact disk ($a = -2$) and an extended wind ($a_w = -0.5$). *From top to bottom*: the inclinations are $i = 30°$ (nearly face-on disk), 45°, 60°, and 75° (nearly edge-on disk). We list the rest of parameters in the notes of Table 4. The color scales are as in Fig. 6.

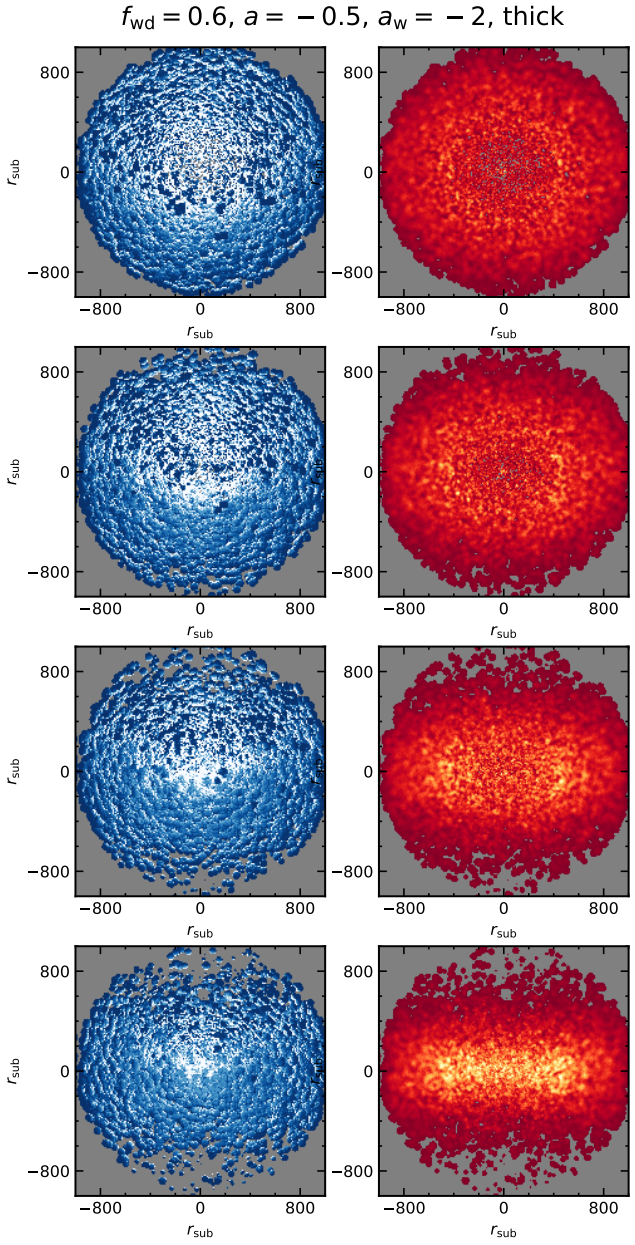

Fig. 9. CAT3D-WIND model images for a "thick" geometry and $f_{wd} = 0.6$ at 8 µm (in blue colors, *left panels*) and 700 µm (in orange colors, *right panels*) for an extended disk ($a = -0.5$) and a compact wind ($a_w = -2$). *From top to bottom*: the inclinations are 30° (nearly face-on disk), 45°, 60°, and 75° (nearly edge-on disk).

The compact disk – wind configuration produces relatively similar morphologies in the mid- and far-IR (see Fig. A.3), with a more roundish shape at lower inclinations and more elongated at higher inclinations, as expected. The mid-IR morphologies of this configuration are similar to those seen in clumpy torus models without a wind component but with similar steep radial dust distributions (see Schartmann et al. 2008).

5.5. The NGC 6814 and NGC 7213 geometry

Figure 10 shows the specific model mid- and far-IR images for NGC 6814 and NGC 7213 at $i = 15°$. In the mid-IR a large fraction of the emission comes from the inner regions of the disk since the radial distribution of the clouds in the disk is moderately steep ($a = -1$). Moreover, because in this model the wind component is not prominent the effects of self-obscuration from the cone walls appear to be small. In the far-IR, the emission is relatively faint and diffuse due to the low number of clouds along the equatorial direction ($N_0 = 5$), and it comes from the outer part of the disk and shows a nearly ring-like morphology.

6. Comparison between CAT3D-WIND model images and observations

The good angular resolutions achieved with ground-based mid-IR instruments on 8−10 m class telescopes and ALMA resolve

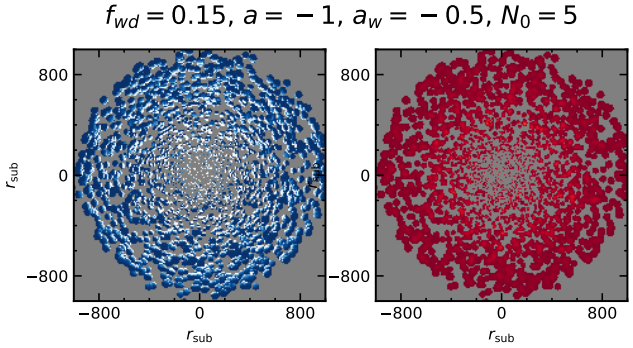

Fig. 10. CAT3D-WIND model images at 8 μm (in blue colors, *left panel*) and 700 μm (in orange colors, *right panel*) for the NGC 7213 and NGC 6814 parameters listed in the fourth column of Table 4 and an inclination of $i = 15°$.

extended components in the mid and far-IR in nearby Seyferts (see Sect. 3.3 and references cited there). In this section we adapt the resolutions of the CAT3D-WIND model images to those of our data, and make a qualitative comparison between models and observations. We refer the reader to Lopez-Rodriguez et al. (2018) and Nikutta et al. (2021) for a similar comparison for NGC 1068 using the Nenkova et al. (2008b) model images produced with HyperCAT.

6.1. Summary of torus and wind properties of the sample

The CAT3D-WIND models produce a diversity of mid and far-IR morphologies (Sects. 5.3–5.5) depending on our viewing angle (inclination) as well as the radial distributions assumed for the disk and wind components and the thickness of the disk and cone walls. In this section we compile values of the torus inclination and sizes as well as the wind properties derived from different types of modeling to aid the comparison between models and observations in Sect. 6.2.

For the torus or disk component, we list in Table 3 the estimated inclinations using fits to the high angular resolution IR SEDs and mid-IR spectroscopy using the CLUMPY models (Nenkova et al. 2008a,b) and fits to the *Spitzer*/IRS spectroscopy with the CAT3D-WIND torus models (Hönig & Kishimoto 2017). We also included the inclination values derived from fits to the X-ray emission using the XCLUMPY model (Tanimoto et al. 2019, 2020; Ogawa et al. 2021). Additionally, there are lower limits to the torus inclination based on the ellipticity of the ALMA extended 870 μm continuum images from GB21. We also provided in this table estimates of the nuclear disk or torus inclination based on the modeling of the ALMA CO(3−2) and CO(2−1) kinematics, and the sizes and PA of the extended 870 μm sizes from GB21.

We additionally summarized in Table 3 some information about the wind/NLR/cones components. In the simplest scenario these components are perpendicular to the nuclear disk or torus. We included the PA of the NLR (see Sect. 3.4 for references), as well as the inclinations and PA of the cones derived from the modeling of the NLR kinematics by Fischer et al. (2013) for the galaxies in common with our work. The constraints on f_{wd} are from González-Martín et al. (2019).

6.2. Fiducial model images for GATOS Seyferts

To match the angular resolutions of the models to those of the observations, we need estimates of r_{sub}. For NGC 1365, recent GRAVITY K-band interferometry derived a radius of 0.035 pc (scaled to our distance) for the hot dust emission (GRAVITY Collaboration 2020b). Using the relationship between the absorption-corrected 2−10 keV luminosity and r_{sub} (Jensen et al. 2017), we obtained values ranging from $r_{sub} = 0.01$ pc for NGC 4941 to $r_{sub} = 0.07$ pc for NGC 7582. We derived another estimate using the radius-luminosity relation seen from GRAVITY observations (GRAVITY Collaboration 2020b), which for the typical bolometric luminosities of our sample provides $r_{sub} = 0.04$ pc. We took this as a representative value for our sample. For NGC 7213 we used the value of $r_{sub} = 0.029$ pc (scaled to our distance) from Hönig et al. (2010) based on K-band reverberation mapping from Kishimoto et al. (2007).

The CAT3D-WIND 2000 r_{sub}×2000 r_{sub} model images cover typical physical sizes of ∼80 pc×80 pc or approximately angular sizes of 1″×1″ for a median distance of 19 Mpc for our galaxies, excluding NGC 6814 and NGC 7213. For these two galaxies, the model images have sizes of ∼60 pc × 60 pc = 0.5″ × 0.5″ at a distance of 23 Mpc. We convolved the 8 μm and 700 μm model images to the typical mid-IR and ALMA far-IR angular resolutions of 0.3″ and 0.1″, respectively, using a Gaussian function. Finally, we resampled the CAT3D-WIND simulated images to representative pixel sizes of ∼0.08″ pixel^{-1} for the mid-IR (0.0453″ pixel^{-1} for NGC 7213) and 0.03″ pixel^{-1} for the far-IR images.

We show a selection of fiducial simulated images for the GATOS Seyferts. In Figs. 11 and 12, we include models with a "thick" geometry and two values of the wind-to-disk ratio $f_{wd} = 0.3$ and $f_{wd} = 0.6$ (compare with the original resolution model images in Sect. 5.4). In Figs. 13 and 14, we display the simulated images for a "thin" geometry with $f_{wd} = 0.6$ (compare with the original resolution model images of Sect. 5.3) and $f_{wd} = 1.2$ (compare with model images in the appendix), respectively. In the next two sections, we describe the morphologies of the fiducial models and make qualitative comparisons with our far-IR and mid-IR observations.

6.2.1. Mid-IR model images

The fiducial mid-IR simulated model images do not show a high level of detail compared to the far-IR. The reasons are twofold. First, most of the mid-IR emission in many of the geometries studied in this work comes from the inner part of the disk and wind. Second, the angular resolution of our mid-IR observations is a factor of three worse than the ALMA ones. Nevertheless, there are some morphological differences in the mid-IR.

The large majority of the CAT3D-WIND model parameters investigated here produces bright and centrally peaked mid-IR emission, which appears unresolved or only slightly resolved at the considered angular resolution. This is most noticeable for compact disk configurations as well as the case of the specific simulation for NGC 6814 and NGC 7213 (left panel of Fig. 15). There is extended mid-IR emission along the polar direction at intermediate inclinations ($i = 45°$) for the extended wind configurations in both "thin" and "thick" geometries with $f_{wd} = 0.6$ and 1.2 (second panels from the top in Figs. 12–14) and the case of a mild extended wind with $f_{wd} = 0.3$ (see Fig. 11) as well as at nearly face-on inclinations ($i = 30°$) for $f_{wd} = 1.2$ (top panels of Fig. 14). Extended mid-IR emission along the equatorial and/or polar direction of the disk is produced at high inclinations in extended disk configurations.

To evaluate the unresolved and extended contribution in the simulated mid-IR model images, we followed a similar

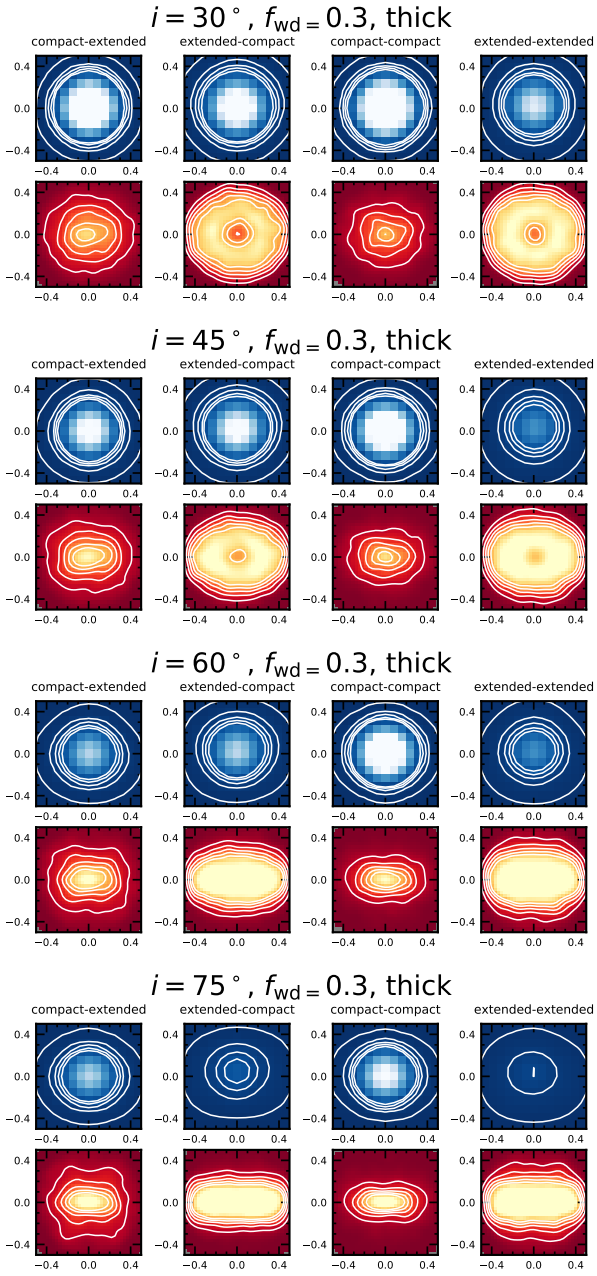

Fig. 11. Simulated CAT3D-WIND images approximately matching the angular resolutions of the observations of the GATOS Seyferts, namely 0.3″ in the mid-IR and 0.1″ in the far-IR. The images cover 1″ × 1″ or 80 pc × 80 pc for the fiducial simulations. The models have a "thick" geometry and a mild wind with a wind-to-disk ratio of $f_{\rm wd}$ = 0.3. For each of the adopted inclinations, the *top panels* are the simulated model images at 8 μm (in blue colors) and the *bottom panels* at 700 μm (in orange colors). The *vertical panels* are the different disk+wind configurations discussed in Sects. 5.3 and 5.4. At a given wavelength, the image brightness scale and the contour levels are the same in all the panels.

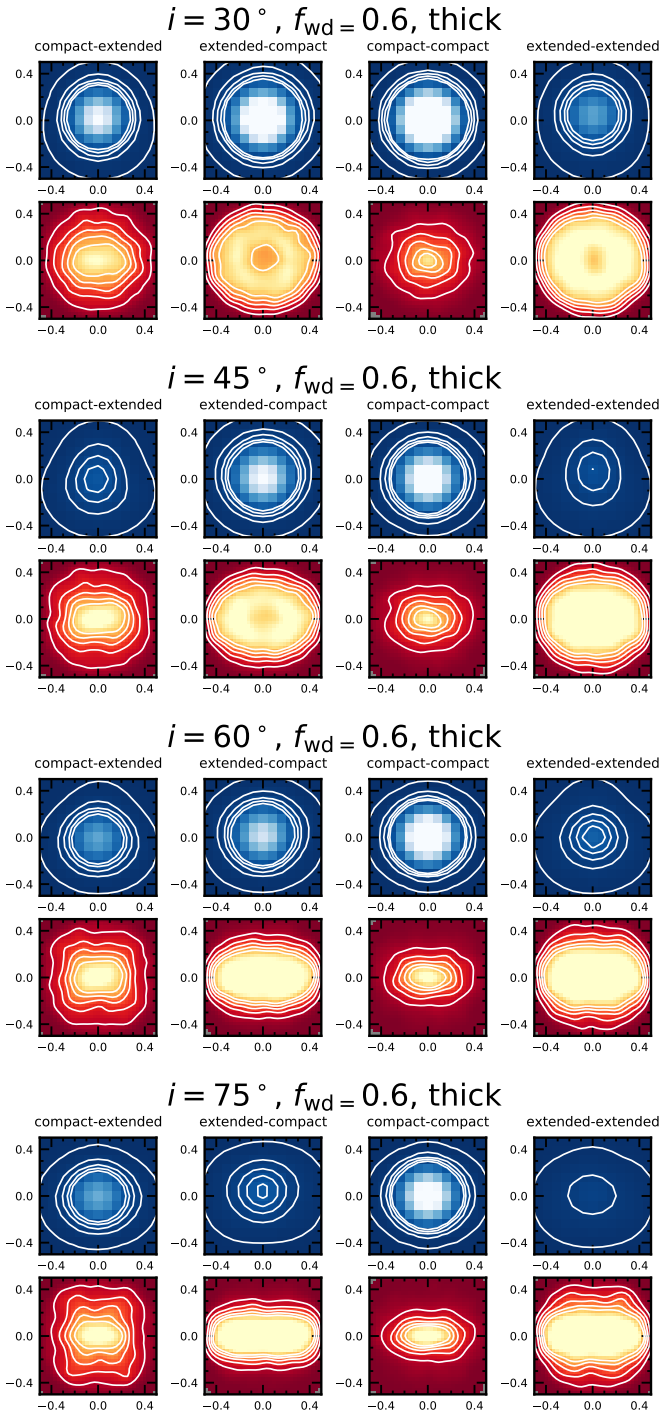

Fig. 12. Simulated CAT3D-WIND images for the GATOS Seyferts. Parameters are as in Fig. 11 but for a wind-to-disk ratio of $f_{\rm wd}$ = 0.6. The image brightness scales and contour levels are as in Fig. 11.

procedure as for the observations in Sect. 3.1. We fit 1D profiles along the equatorial and polar directions. For the unresolved component, we fixed the Gaussian width to the value used to convolve the original CAT3D-WIND images. With the scaling factors derived from these fits, we subtracted the PSF image from the fiducial mid-IR model images.

Rather than fitting the individual galaxies, in Figs. 16–19 we show some model examples of the different observed mid-IR morphologies. The case of unresolved plus two-sided polar mid-IR emission (Fig. 16) is seen in a compact disk – extended wind "thin" geometry with a high wind-to-disk ratio ($f_{\rm wd}$ = 0.6, in the figure), at an intermediate inclination of i = 45°. These parameters are based on the constraints for NGC 1365, including the relatively compact torus seen with ALMA (see Table 3). The 1D profiles and PSF-subtracted model image show that the extended component is more relevant along the polar direction.

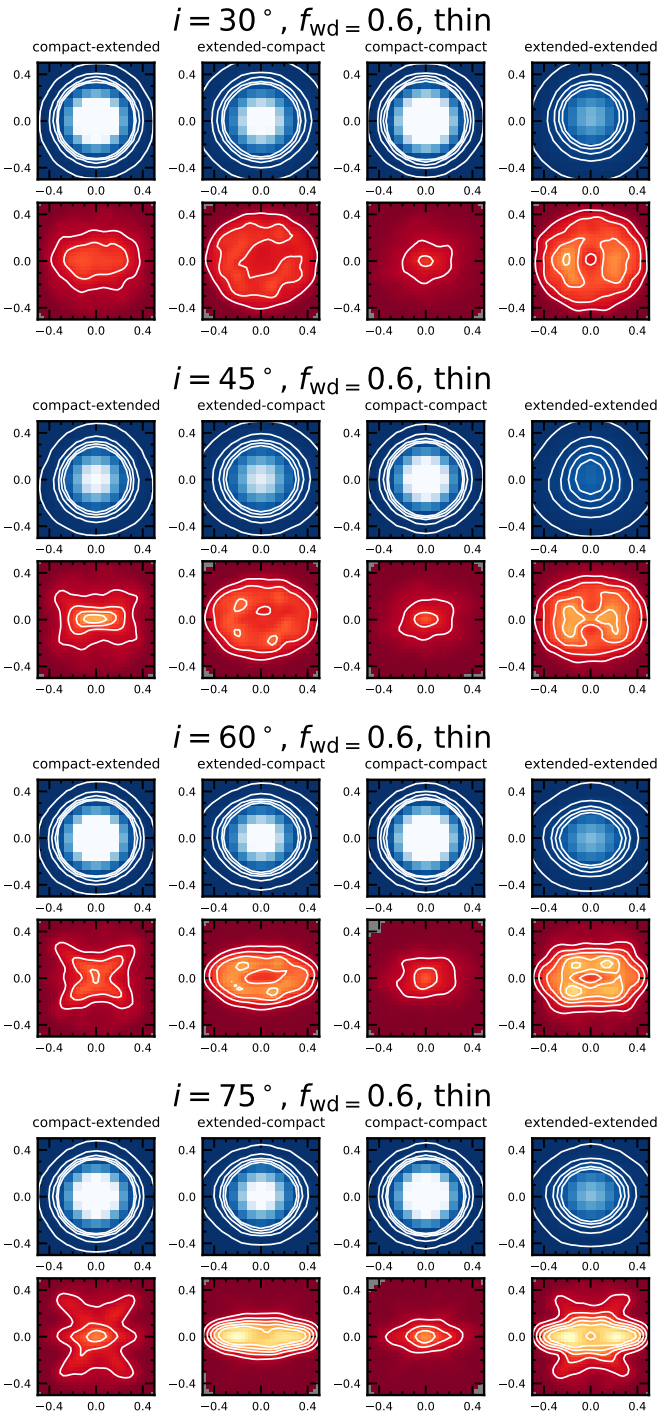

Fig. 13. Simulated CAT3D-WIND model images for angular resolutions approximately representing those of the GATOS Seyfert observations. Parameters are as in Fig. 12 but for a "thin" geometry. The image brightness scales and contour levels are as in Fig. 11.

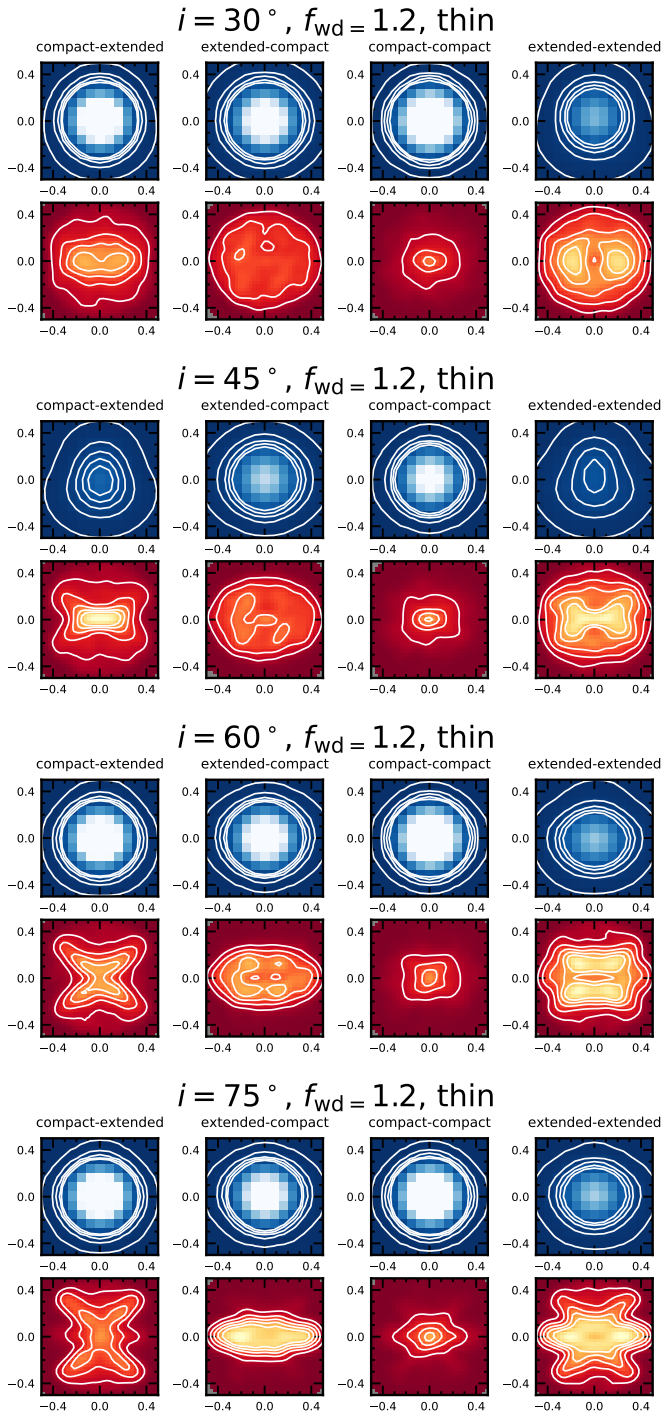

Fig. 14. Simulated CAT3D-WIND images matching for the GATOS Seyferts. Parameters are the same as in Fig. 13 but for a wind-to-disk ratio of $f_{wd} = 1.2$. The image brightness scales and contour levels are as in Fig. 11.

The unresolved plus one-sided polar mid-IR emission (Fig. 17) is seen mostly at intermediate inclinations ($i = 45°$ in the figure) in the simulated image and profiles, for extended disk – extended wind configurations with a "thick" geometry. Low to intermediate wind-to-disk values ($f_{wd} = 0.3$ in the figure) are needed to have an important contribution from the unresolved mid-IR emission, as seen in our observations of NGC 3227 and NGC 7582.

The combination of unresolved plus equatorial mid-IR emission (Fig. 18) is observed at higher inclinations ($i = 75°$ in the figure) with a "thick" geometry and extended disk and compact wind ($f_{wd} = 0.3$ in the figure). The PSF-subtracted mid-IR model image shows a morphology consistent with the observations of NGC 6300. Finally, we checked models that produce nearly unresolved mid-IR morphologies (Fig. 19) such as a "thick" geometry and extended disk and compact wind with $f_{wd} = 0.3$ in the figure for an inclination of $i = 60°$. This would reproduce

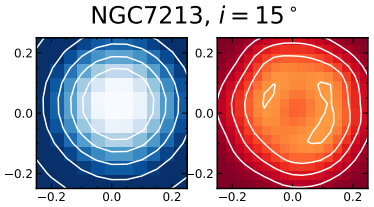

Fig. 15. Simulated CAT3D-WIND model images at 8 μm (*left*, blue colors) and 700 μm (*right*, orange colors) with the parameters of Fig. 10 approximately matching the angular resolution of NGC 7213.

the case of NGC 7314 which has a large 870 μm torus but mostly unresolved mid-IR emission.

6.2.2. Far-IR model images

All the simulated far-IR model images are resolved and show a variety of morphologies. This is in excellent agreement with the observational result that the extended ALMA 870 μm emission in most GATOS Seyferts dominates the total emission at this wavelength (see GB21 for more details). At low-to-intermediate inclinations, the far-IR simulated model images with extended disk components show ring-like morphologies. As expected, the compact disk configurations show a more compact far-IR morphology. At high inclinations and extended wind configurations, the characteristic "X"-shape, which is due to the edge brightening in the cone walls, is seen in the "thin" geometry and high values of the wind-to-disk cloud ratio (the two bottom panels of Figs. 13 and 14, that is, for $i = 60$ and 75°). It is also seen, although with low contrast, for $f_{\rm wd} = 0.3$–0.6 and "thick" geometries (Figs. 11 and 12). The ALMA 870 μm images of a few GATOS Seyferts are suggestive of this "X"-shape, for instance, NGC 5643, NGC 7314, and especially in NGC 7582 (see Figs. 2–4 in GB21 and Fig. 3). NGC 4388 shows mixed/polar emission at 870 μm. A compact disk and compact wind "thick" configuration with a low wind-to-disk ratio and seen at an intermediate inclination reproduces well the observed morphology.

We show the specific simulation for NGC 7213 in Fig. 15 (right panel), which is also valid for NGC 6814. The far-IR model image shows a ring-like geometry due to the low inclination of $i = 15°$ and the $a = -1$ cloud radial distribution in the disk. The ALMA extended 870 μm emission of NGC 6814 and NGC 7213 (Fig. 3 in GB21) shows centrally peaked emission. As discussed by GB21, it is possible that a large fraction of this emission is not associated with cold dust. This was based on the discrepancies between the molecular gas masses derived from the CO(3−2) and the 870 μm emission.

7. Discussion

The emerging picture for the central regions of radio-quiet AGNs has the obscuring torus as part of a gas flow cycle where gas is brought in from the host galaxy and then driven out by the AGN in a wind (see Elitzur & Shlosman 2006). High angular resolution observations gathered over the last 15 years point to a multiphase multicomponent structure where both the torus and the base of the wind can contribute to the AGN obscuration (see the review by Ramos Almeida & Ricci 2017). Recently Hönig (2019) used simple physical principles to support this new unifying view in a disk+wind scenario. Up until now, this view was based on observations of a few individual AGN. GATOS aims for a comprehensive study of the nuclear activity and its connection with the host galaxy in a well-defined sample of nearby Seyfert galaxies.

7.1. Observational considerations

One of the main caveats from the analysis of the extended mid-IR emission with ground-based facilities is the stability of the PSF. Observing conditions can change on scales of a few minutes and affect the shape of the PSF, which we took from the emission of a standard star observed close in time. This combined with the modest sensitivity to diffuse emission due to the high thermal background make it challenging to derive the morphologies of the extended mid-IR emission in the vicinity of the unresolved AGN emission. Nevertheless, we detected extended mid-IR emission in seven of the twelve Seyfert galaxies analyzed in this work, with sizes between 50 and 160 pc.

The measured orientations of the extended mid-IR emission are approximately along the polar/NLR direction and perpendicular to the ALMA-identified tori (Fig. 3) in five galaxies (NGC 1365, NGC 3227, NGC 5643, and NGC 7582, and tentatively in NGC 4388) as well as the inner regions of NGC 5506 (see also Asmus 2019). In NGC 5506, NGC 5643, and NGC 6300, there is also extended mid-IR emission along the equatorial direction of the torus and/or the host galaxy, adding to the complexity of the dust emission. The extended mid-IR emission along the polar direction is likely associated with AGN-driven dusty outflows (Wada et al. 2018; Williamson et al. 2020; Venanzi et al. 2020) and/or dust located in the edges of the NLR and ionization cones. With the existing data, we cannot distinguish between the two possibilities. We note that contributions from emission lines in the imaging filters, in particular [Ne II] 12.8 μm in NGC 5643 and NGC 7582, might be partly responsible for the alignment along the polar direction. However, there are galaxies in our sample with relatively bright optical NLR emission and faint or no extended polar mid-IR emission.

7.2. The role of the IR radiation pressure

In the immediate surroundings of an active nucleus, the gas and dust are subject to the AGN radiation pressure. In particular, the AGN IR radiation pressure may play a significant role in both maintaining the vertical extent of the torus and launching dusty outflows (Pier & Krolik 1992b; Krolik 2007; Fabian et al. 2008; Venanzi et al. 2020; Tazaki & Ichikawa 2020). We investigated the observed mid-IR morphologies of our sample in the context of the Venanzi et al. (2020) semi-analytical disk+wind models, which include the AGN radiation pressure, gravity from the central black hole, and the IR radiation pressure. They showed that dusty outflows are launched more efficiently when the IR radiation pressure is the dominant component. This takes place when the AGN radiation pressure balances gravity from the central black hole.

We found that those Seyferts with polar mid-IR emission show intermediate nuclear hydrogen column densities ($\log N_{\rm H} \simeq 22.5$–$23\,{\rm cm}^{-2}$) and moderate Eddington ratios ($\log \lambda_{\rm Edd} \simeq -1$ to -1.75). As can be seen from Fig. 4, the observed nuclear column densities and Eddington ratios place them close to the region where the IR radiation pressure is most effective. However, polar outflows are also possible at high nuclear column densities for sufficiently high Eddington ratios, as is the case of NGC 1068 and even Circinus. The dashed line plotted in Fig. 4 is thus not a hard boundary, but rather it indicates the combination

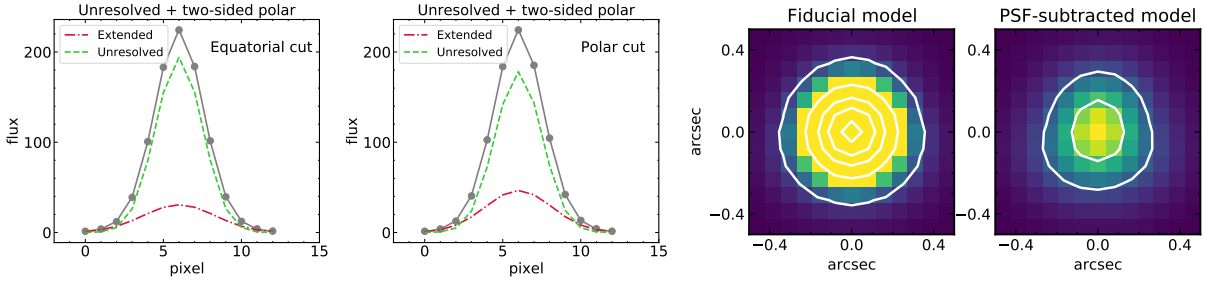

Fig. 16. *Two mostleft panels*: equatorial and polar 1D profiles for a CAT3D-WIND simulated galaxy image at 8 μm with the typical resolutions of our mid-IR observations. The model parameters are: a compact disk – extended wind, "thin" geometry with $f_{\rm wd} = 0.6$ at $i = 45°$. The dashed and dashed-dotted lines are the fit unresolved and extended components, respectively, and the solid lines the sum of both. *Two mostright panels*: mid-IR fiducial model image and the PSF-subtracted model image, respectively.

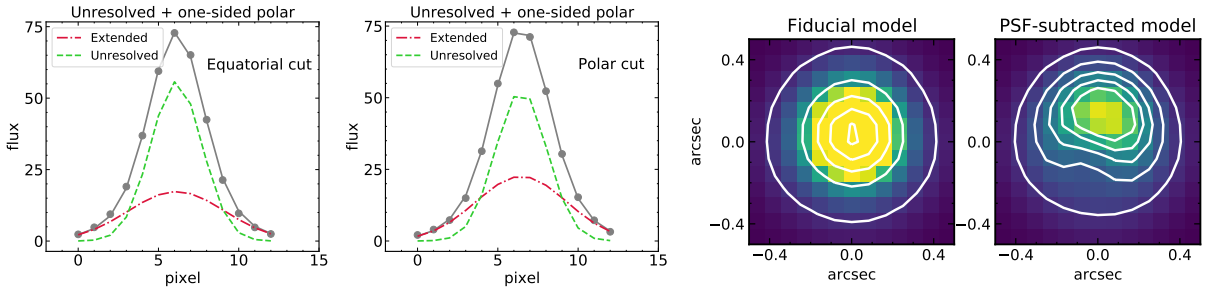

Fig. 17. Same as Fig. 16, but for an extended disk – extended wind, "thick" geometry model with $f_{\rm wd} = 0.3$ at $i = 45°$.

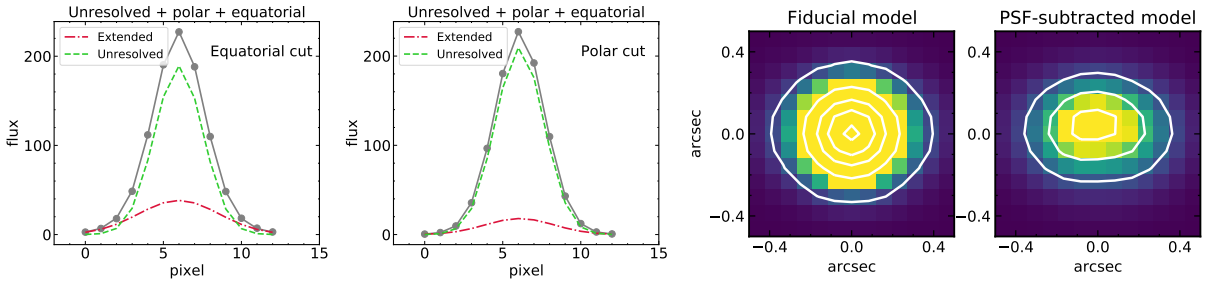

Fig. 18. Same as Fig. 16, but for a compact disk – compact wind, "thick" geometry model with $f_{\rm wd} = 0.3$ at $i = 75°$.

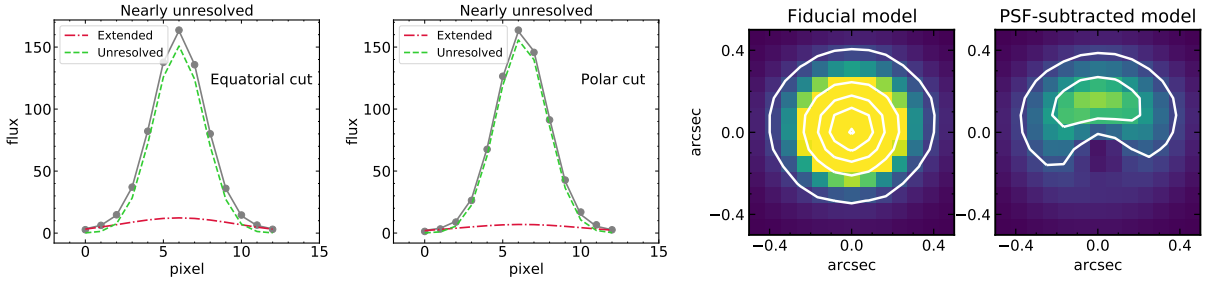

Fig. 19. Same as Fig. 16, but for an extended disk – compact wind, "thick" geometry model with $f_{\rm wd} = 0.3$ at $i = 60°$.

of Eddington ratios and column densities where the IR radiation pressure dominates for individual clouds. The well-studied case of Circinus illustrates this. Indeed, Venanzi et al. (2020) used their simulations and predicted a disk plus wind distribution for this galaxy, in good agreement with both observations (Packham et al. 2005a) and the radiative transfer modeling done by Stalevski et al. (2017).

Molecular outflows at the torus or its vicinity (tens of parsecs) are observed in some nearby Seyferts (see Gallimore et al. 2016; Izumi et al. 2018; Alonso-Herrero et al. 2019; García-Burillo et al. 2019), and are also predicted by hydrodynamic simulations of radiation-driven winds (Wada et al. 2016; Williamson et al. 2020). In addition, the AGN in Fig. 4 in the region where outflows are launched also show strong evidence for the clearing of (cold) molecular gas in the nuclear regions, possibly related to these nuclear outflows (see GB21 and also Alonso-Herrero et al. 2019). We also note that in some Seyfert galaxies (for instance, NGC 1068) the radio jet may also play a role in maintaining or even boosting radiation-driven outflows. This is particularly true, when the

molecular outflows occur at 100 pc scales far from the scales where the IR radiation of the torus dominates (that is, near the sublimation radius, see Venanzi et al. 2020).

Seyferts with both polar and equatorial mid-IR emission have moderate-to-low Eddington ratios ($\log \lambda_{\rm Edd} \simeq -1.3$ to -2.5), and high column densities ($\log N_{\rm H} \gtrapprox 23\,{\rm cm}^{-2}$). As shown by Venanzi et al. (2020), these conditions might be more conducive to equatorial dusty outflows (see Alonso-Herrero et al. 2018) since large column densities might suppress the liftup of material. The galaxies with little or no extended mid-IR emission are the least luminous in terms of their 2−10 keV luminosities, typically below $\sim 1.5 \times 10^{42}$ erg s^{-1}. In Fig. 4 they are in regions of this diagram where dusty outflows are not expected, either because they are close to the blowout region or their Eddington ratios are very low. In the scenario proposed by GB21, these are galaxies where we would not expect to see the imprint of AGN feedback from nuclear outflows.

The predictions of the models used above regarding the behavior of outflows as a function of location in the $N_{\rm H}$−$\lambda_{\rm Edd}$ space should only be taken as broad characterizations, rather than as strict laws. Venanzi et al. (2020) represented clouds as indivisible particles, while Fabian et al. (2008) represented the entire gas distribution as a thick spherically symmetric shell. However, any optically thick cloud experiencing radiation pressure that is, above the effective Eddington limit for dusty gas will fragment through the radiative Rayleigh-Taylor instability into fingers of low density outflow and high density inflow (Jacquet & Krumholz 2011; Zhang et al. 2018). Finally, winds do not need to be launched as polar winds to obtain a polar outflow. The anisotropy of the AGN emission, combined with anisotropic extinction from a torus, causes more equatorial outflows feel less radiation pressure and are more likely to fail, even if they are injected at the same speed (Williamson et al. 2020). Thus, non-polar outflows are therefore likely to evolve into polar outflows. Anisotropy and gas instabilities together mean that outflows and inflows can exist (and even coexist) across a wide range of inclinations, column densities, and Eddington factors. Further observations and simulations are needed to better constrain the necessary parameters for a polar outflow.

7.3. Disk+wind models

The CAT3D-WIND models capture qualitatively the expected dust and gas configurations predicted by simulations of dusty disks (see Figs. 10–12 of Venanzi et al. 2020) and/or dust in the NLR walls illuminated by the AGN. Moreover, the wind-to-disk cloud ratio in the CAT3D-WIND models can also be associated qualitatively with feedback effects seen observationally in our sample at high AGN luminosities and/or Eddington ratios (see GB21). Out of the large parameter space of the CAT3D-WIND models, in this work we selected parameter ranges based on results from fitting the *Spitzer*/IRS spectra (González-Martín et al. 2019) for several GATOS Seyferts. Additionally, we distributed the dust in the models over characteristic physical sizes of 2000 $r_{\rm sub}$. These were motivated by the ALMA resolved molecular dusty tori of our sample (GB21) as well as the presence of extended mid-IR components. However, we emphasize that the dust emission is from a disk+wind configuration, and any additional dust is not treated in the picture, but it may exist in reality.

We showed in Sect. 6 that to make meaningful comparisons between the CAT3D-WIND model images and observations, even if only qualitatively, it is necessary to convolve and resample the models to the typical angular resolutions and pixel sizes. The level of morphological detail in the mid- and far-IR as well as the unresolved mid-IR emission fractions depend on the assumed sublimation radius. If we adopted a factor of two smaller sublimation radius ($r_{\rm sub} = 0.02$ pc) for the fiducial models, the simulated images would cover typically 40 pc × 40 pc or approximately 0.5″ × 0.5″. In those mid-IR models dominated by the point source, a larger fraction of the mid-IR emission would be unresolved. Detailed morphological comparisons on a case-by-case basis require accurate estimates of the sublimation radius as well as higher angular resolution observations, especially in the mid-IR.

In the fiducial CAT3D-WIND models produced for our sample, we found that the mid-IR emission comes mainly from the inner part of the disk and cone for all values of the wind-to-disk cloud ratios and all inclinations. Extended biconical and one-sided polar mid-IR emission becomes more apparent in the extended-wind configurations at $f_{\rm wd} \geq 0.6$. The latter morphology is present mostly at intermediate inclinations in the "thick" geometry because of the disk and cone wall obscuration. Torus models without a wind component also give rise to similar one-sided mid-IR morphologies due to self obscuration (see e.g., Siebenmorgen et al. 2015; Lopez-Rodriguez et al. 2018; Nikutta et al. 2021).

To reproduce the relatively large contributions from the unresolved component seen in the mid-IR at our resolution requires low to moderate values of the wind-to-dust ratio ($f_{\rm wd} = 0.3$−0.6) in most GATOS Seyferts. We also note, that although clumpiness introduces some inhomogeneities, the CAT3D-WIND models produce mostly symmetric (with respect to the wind axis) wind/hollow cone morphologies. For several bright nearby AGN the polar extension observed in the mid-IR is preferentially tilted toward one side of the ionization cone and countercone, similarly to observations of the NLR. Circinus is one of the best examples of this (see Packham et al. 2005a; Stalevski et al. 2017). This could be just a sign of general inhomogeneity of outflows (Wada et al. 2016, 2018) or a slight misalignment of accretion disk and dust disk from where the winds are driven, as proposed by Stalevski et al. (2017).

The observed ALMA 870 µm disk-like morphologies and extents of the GATOS Seyferts are reproduced qualitatively with the simulated CAT3D-WIND model images, including those with a dominant equatorial torus emission as well as the small number of galaxies with far-IR along the polar direction. The characteristic "X"-shape associated with the dusty winds (see e.g., Wada et al. 2016; Williamson et al. 2020) is seen at intermediate to edge-on inclinations in the extended disk and wind model configurations. Furthermore, this morphology is appreciated better for higher values of $f_{\rm wd}$ and thin cone walls, and in the far-IR rather than the mid-IR. In a few Seyferts in our sample (NGC 5643, NGC 7314, and NGC 7582), there is some evidence of this "X"-shape.

Observationally, the clearest example of an "X"-shape morphology is observed in the HCO+(4−3) dense molecular gas emission of NGC 1068 (see Figs. 11 and 12 of García-Burillo et al. 2019). Moreover, at 432 µm the torus of NGC 1068 is resolved in the equatorial direction but it also shows a polar elongation (García-Burillo et al. 2016), as in the simulations. The dusty torus or disk may spread over larger regions (diameter of ∼60 pc), as traced by near-IR scattered light (Gratadour et al. 2015). The sublimation radius of $r_{\rm sub} = 0.1$−0.2 pc and torus diameter of 20−60 pc of NGC 1068 mean that in a CAT3D-WIND model the dust should be distributed over a region of ∼300−600 $r_{\rm sub}$ in diameter, but mostly concentrated toward the smaller region probed by the ALMA

continuum. The polar component in the mid-IR is more extended and brighter to the north of the AGN (Tomono et al. 2001). For the estimated $i = 70°$ (García-Burillo et al. 2019), a model with a compact disk – extended wind configuration and a "thin" geometry reproduces all these observations (Fig. 13). Higher angular resolution ALMA continuum images are needed for NGC 1068 and other nearby Seyferts to confirm the "X"-shape morphologies.

8. Summary

In this work, we analyzed high-angular (∼0.3″) mid-IR imaging observations of 12 GATOS Seyferts and compared them with the ALMA observations from Paper I (GB21). We assessed the observations in the context of the Venanzi et al. (2020) semi-analytical models which include the AGN radiation pressure, gravity from the central black hole, and the IR radiation pressure. Motivated by the observed mid- and far-IR morphologies in our sample, we generated new radiative transfer CAT3D-WIND models (Hönig & Kishimoto 2017) and 8 μm, 12 μm, and 700 μm model images (see Figs. 6–10 and appendix). We made an informed choice of the model parameters (see Table 4) using the fits of the *Spitzer*/IRS spectra from González-Martín et al. (2019) for the GATOS Seyferts in their sample. Thus, we tailored the models to the properties of the GATOS Seyferts analyzed in this work, which are representative of X-ray selected AGN with median luminosities $L(2-10\,\mathrm{keV}) = 2 \times 10^{42}\,\mathrm{erg\,s^{-1}}$. We distributed the dust in a disk+wind geometry over a $2000\,r_{\mathrm{sub}} \times 2000\,r_{\mathrm{sub}}$ region to account for the relatively large torus sizes observed with ALMA in our sample. We included compact and extended configurations for the disk and wind, "thin" and "thick" geometries for the disk and cone walls, and a range of wind-to-disk cloud ratios.

Our main results are the following:

- In seven out of the twelve galaxies, we detected extended mid-IR emission with sizes between 50 and 160 pc (Fig. 2). The other five galaxies only show faint extended or mostly unresolved mid-IR emission. At our current mid-IR angular resolutions, however, the unresolved emission contributes between 60% and 100% of the nuclear 1.5″ ∼ 150 pc emission in the majority of the sources.
- There is a diversity of nuclear extended mid-IR morphologies. In six galaxies there is extended mid-IR emission approximately in the polar direction and perpendicular to the extended 870 μm component detected with ALMA. The latter continuum emission traces the equatorial component of the dusty molecular torus in the majority of the GATOS Seyferts (GB21). The only exception is NGC 6300 where the extended mid-IR is along the equatorial direction of the torus and dust in the host galaxy. In some galaxies there are other extended mid-IR components associated with emission in the host galaxy and/or star formation.
- The majority of galaxies in our sample with extended mid-IR emission show intermediate-to-high nuclear column densities ($\log N_{\mathrm{H}}\,(\mathrm{ALMA}) \sim 22.5-23.9\,\mathrm{cm^{-2}}$) and moderate Eddington ratios ($\log \lambda_{\mathrm{Edd}} \simeq -1.9$ to -1.2) and have $L(2-10\,\mathrm{keV}) > 1.5 \times 10^{42}\,\mathrm{erg\,s^{-1}}$. According to the simulations of Venanzi et al. (2020), these conditions are favorable to launching dusty winds (Fig. 4), both in the polar and equatorial direction.
- At our mid-IR 0.3″ resolutions, the fiducial CAT3D-WIND models show unresolved or only slightly resolved mid-IR emission in a significant number of model configurations (Figs. 11–15). Polar mid-IR emission is observed at intermediate inclinations, extended wind configurations, and intermediate-to-high wind-to-disk cloud ratios. To reproduce the observed mid-IR unresolved/extended fractions in our galaxies, low-to-moderate wind-to-disk ratios are needed (up to $f_{\mathrm{wd}} \sim 0.6$).
- At our ALMA 0.1″ resolution, the fiducial CAT3D-WIND model images show resolved far-IR morphologies, trace well the extent of the dust distribution, and reproduce the observed morphologies. In the models, the "X"-shape morphologies associated with a strong and extended wind component are seen at this resolution for high inclinations and are more apparent in the far-IR. While there is some ALMA observational evidence for these in our sample, higher angular resolution data are needed.

In conclusion, this work together with GB21 provide observational support for the torus+wind scenario. Dusty nuclear winds with the accompanying polar dust emission and possibly with ongoing clearing of the nuclear regions might be common in Seyferts with high Eddington ratios and/or AGN luminosities (see also Ricci et al. 2017a; González-Martín et al. 2019). At moderate Eddington ratios, if the nuclear column densities are high, the IR radiation pressure uplift may be suppressed and only equatorial dusty outflows could occur (Venanzi et al. 2020). GB21 also showed that (radio-quiet) AGN with low Eddington ratios and/or luminosities might be dominated by the disk or torus component, and have higher covering factors (Ezhikode et al. 2017; Ricci et al. 2017a; González-Martín et al. 2019). These are predicted to show little or no polar dust emission, as confirmed by our observations.

In the near future, the Mid-Infrared Instrument (MIRI, Rieke et al. 2015; Wright et al. 2015) onboard the *James Webb* Space Telescope will provide observations at angular resolutions ($FWHM \sim 0.3''$ at 8 μm) similar to those of the ground-based mid-IR imaging observations analyzed in this work. MIRI high sensitivity and spectral coverage, and especially the stability of the PSF will enable for the separation of the emitting components in the nuclear regions of AGN. The next generation of near- and mid-IR instruments on 30–40 m-class ground-based telescopes (Packham et al. 2018; Brandl et al. 2021; Davies et al. 2021; Thatte et al. 2021) will allow observations of nearby Seyfert galaxies at angular resolutions in the tens of milli-arcsecond range that are comparable to the best resolutions currently achieved with ALMA. All these instruments will provide an unprecedented IR view of the dust emission and gas cycle in the immediate surroundings of nearby AGN. Finally, the comparison between models and observations will benefit from accurate estimates of the sublimation radii, dust composition, and the inclusion of the circumnuclear environment.

Acknowledgements. We thank D. Asmus, M. Villar-Martín, and M. Venanzi for interesting discussions. AA-H and SG-B acknowledge support through grant PGC2018-094671-B-I00 (MCIU/AEI/FEDER,UE). AA-H, AL, and MP-S work was done under project No. MDM-2017-0737 Unidad de Excelencia "María de Maeztu" – Centro de Astrobiología (INTA-CSIC). SG-B thanks support from the research project PID2019-106027GA-C44 from the Spanish Ministerio de Ciencia e Innovación. SFH acknowledges support by the EU Horizon 2020 framework programme via the ERC Starting Grant DUST-IN-THE-WIND (ERC-2015-StG-677117). IGB acknowledges support from STFC through grant ST/S000488/1. CRA acknowledges financial support from the Spanish Ministry of Science, Innovation and Universities (MCIU) under grant with reference RYC-2014-15779, from the European Union's Horizon 2020 research and innovation programme under Marie Skłodowska-Curie grant agreement No 860744 (BiD4BESt), from the State Research Agency (AEI-MCINN) of the Spanish MCIU under grants "Feeding and feedback in active galaxies" with reference PID2019-106027GB-C42 and "Quantifying the impact of quasar feedback on galaxy evolution (QSOFEED)" with reference EUR2020-112266. CRA also acknowledges support from the Consejería de Economía, Conocimiento y Empleo del Gobierno de Canarias and the European Regional

Development Fund (ERDF) under grant with reference ProID2020010105 and from IAC project P/301404, financed by the Ministry of Science and Innovation, through the State Budget and by the Canary Islands Department of Economy, Knowledge and Employment, through the Regional Budget of the Autonomous Community. OG-M acknowledges support from UNAM PAPIIT IN105720. AJB has received funding from the European Research Council (ERC) under the European Union's Horizon 2020 Advanced Grant 789056 "First Galaxies". AA-H and AJB acknowledge support from a Royal Society International Exchange Grant. BG-L acknowledges support from the Spanish Agencia Estatal de Investigación del Ministerio de Ciencia e Innovación (AEI-MCINN) under grant with reference PID2019-107010GB-I00. TI is supported by Japan Society for the Promotion of Science (JSPS) KAKENHI grant No. JP20K14531. AL acknowledges the support from Comunidad de Madrid through the Atracción de Talento Investigador Grant 2017-T1/TIC-5213, and PID2019-106280GB-I00 (MCIU/AEI/FEDER,UE). MPS acknowledges support from the Comunidad de Madrid through the Atracción de Talento Investigador Grant 2018-T1/TIC-11035 and PID2019-105423GA-I00 (MCIU/AEI/FEDER,UE). DR acknowledges support from the Oxford Fell Fund and STFC through grant ST/S000488/1. DJR acknowledges support from the STFC (ST/T000244/1). MS is supported by the Ministry of Education, Science and Technological Development of the Republic of Serbia through the contract no. 451-03-9/2021-14/200002 and the Science Fund of the Republic of Serbia, PROMIS 6060916, BOWIE. Based on observations made with the Gran Telescopio Canarias (GTC), installed at the Spanish Observatorio del Roque de los Muchachos of the Instituto de Astrofísica de Canarias, in the island of La Palma. Based on observations collected at the European Organisation for Astronomical Research in the Southern Hemisphere. Based on observations obtained at the international Gemini Observatory, a program of NSF's NOIRLab, which is managed by the Association of Universities for Research in Astronomy (AURA) under a cooperative agreement with the National Science Foundation on behalf of the Gemini Observatory partnership: the National Science Foundation (United States), National Research Council (Canada), Agencia Nacional de Investigación y Desarrollo (Chile), Ministerio de Ciencia, Tecnología e Innovación (Argentina), Ministério da Ciência, Tecnologia, Inovações e Comunicações (Brazil), and Korea Astronomy and Space Science Institute (Republic of Korea). This paper makes use of the following ALMA data: ADS/JAO.ALMA#2017.1.00082.S and #2018.1.00113.S. ALMA is a partnership of ESO (representing its member states), NSF (USA) and NINS (Japan), together with NRC (Canada) and NSC and ASIAA (Taiwan), in cooperation with the Republic of Chile. The Joint ALMA Observatory is operated by ESO, AUI/NRAO and NAOJ. The National Radio Astronomy Observatory is a facility of the National Science Foundation operated under cooperative agreement by Associated Universities, Inc. This research has made use of the NASA/IPAC Extragalactic Database (NED), which is operated by the Jet Propulsion Laboratory, California Institute of Technology, under contract with the National Aeronautics and Space Administration. This research made use of Astropy (`http://www.astropy.org`), a community-developed core Python package for Astronomy (Astropy Collaboration 2013, 2018). IRAF is distributed by the National Optical Astronomy Observatory, which is operated by the Association of Universities for Research in Astronomy (AURA) under a cooperative agreement with the National Science Foundation.

References

Alonso-Herrero, A., Ramos Almeida, C., Mason, R., et al. 2011, ApJ, 736, 82
Alonso-Herrero, A., Sánchez-Portal, M., Ramos Almeida, C., et al. 2012, MNRAS, 425, 311
Alonso-Herrero, A., Esquej, P., Roche, P. F., et al. 2016, MNRAS, 455, 563
Alonso-Herrero, A., Pereira-Santaella, M., García-Burillo, S., et al. 2018, ApJ, 859, 144
Alonso-Herrero, A., García-Burillo, S., Pereira-Santaella, M., et al. 2019, A&A, 628, A65
Alonso-Herrero, A., Pereira-Santaella, M., Rigopoulou, D., et al. 2020, A&A, 639, A43
Antonucci, R. 1993, ARA&A, 31, 473
Asmus, D. 2019, MNRAS, 489, 2177
Asmus, D., Hönig, S. F., Gandhi, P., Smette, A., & Duschl, W. J. 2014, MNRAS, 439, 1648
Asmus, D., Hönig, S. F., & Gandhi, P. 2016, ApJ, 822, 109
Astropy Collaboration (Robitaille, T. P., et al.) 2013, A&A, 558, A33
Astropy Collaboration (Price-Whelan, A. M., et al.) 2018, AJ, 156, 123
Baumgartner, W. H., Tueller, J., Markwardt, C. B., et al. 2013, ApJS, 207, 19
Brandl, B., Bettonvil, F., van Boekel, R., et al. 2021, The Messenger, 182, 22
Burtscher, L., Meisenheimer, K., Tristram, K. R. W., et al. 2013, A&A, 558, A149
Cameron, M., Storey, J. W. V., Rotaciuc, V., et al. 1993, ApJ, 419, 136
Combes, F., García-Burillo, S., Audibert, A., et al. 2019, A&A, 623, A79
Davies, R. I., Maciejewski, W., Hicks, E. K. S., et al. 2014, ApJ, 792, 101
Davies, R., Hörmann, V., Rabien, S., et al. 2021, The Messenger, 182, 17
Domínguez-Fernández, A. J., Alonso-Herrero, A., García-Burillo, S., et al. 2020, A&A, 643, A127
Efstathiou, A., & Rowan-Robinson, M. 1995, MNRAS, 273, 649
Efstathiou, A., Hough, J. H., & Young, S. 1995, MNRAS, 277, 1134
Elitzur, M., & Shlosman, I. 2006, ApJ, 648, L101
Erroz-Ferrer, S., Carollo, C. M., den Brok, M., et al. 2019, MNRAS, 484, 5009
Ezhikode, S. H., Gandhi, P., Done, C., et al. 2017, MNRAS, 472, 3492
Fabian, A. C., Vasudevan, R. V., & Gandhi, P. 2008, MNRAS, 385, L43
Ferruit, P., Wilson, A. S., & Mulchaey, J. 2000, ApJS, 128, 139
Fischer, T. C., Crenshaw, D. M., Kraemer, S. B., & Schmitt, H. R. 2013, ApJS, 209, 1
Fritz, J., Franceschini, A., & Hatziminaoglou, E. 2006, MNRAS, 366, 767
Fuller, L., Lopez-Rodriguez, E., Packham, C., et al. 2019, MNRAS, 483, 3404
Gallagher, S. C., Everett, J. E., Abado, M. M., & Keating, S. K. 2015, MNRAS, 451, 2991
Gallimore, J. F., Elitzur, M., Maiolino, R., et al. 2016, ApJ, 829, L7
García-Bernete, I., Ramos Almeida, C., Acosta-Pulido, J. A., et al. 2016, MNRAS, 463, 3531
García-Bernete, I., Ramos Almeida, C., Alonso-Herrero, A., et al. 2019, MNRAS, 486, 4917
García-Bernete, I., Alonso-Herrero, A., García-Burillo, S., et al. 2021, A&A, 645, A21
García-Burillo, S., Combes, F., Ramos Almeida, C., et al. 2016, ApJ, 823, L12
García-Burillo, S., Combes, F., Ramos Almeida, C., et al. 2019, A&A, 632, A61
Garcia-Burillo, S., Alonso-Herrero, A., Ramos Almeida, C., et al. 2021, A&A, 652, A98
García-González, J., Alonso-Herrero, A., Hönig, S. F., et al. 2017, MNRAS, 470, 2578
González-Martín, O., Masegosa, J., García-Bernete, I., et al. 2019, ApJ, 884, 11
Granato, G. L., & Danese, L. 1994, MNRAS, 268, 235
Gratadour, D., Rouan, D., Grosset, L., Boccaletti, A., & Clénet, Y. 2015, A&A, 581, L8
GRAVITY Collaboration (Pfuhl, O., et al.) 2020a, A&A, 634, A1
GRAVITY Collaboration (Dexter, J., et al.) 2020b, A&A, 635, A92
Hönig, S. F. 2019, ApJ, 884, 171
Hönig, S. F., & Kishimoto, M. 2010, A&A, 523, A27
Hönig, S. F., & Kishimoto, M. 2017, ApJ, 838, L20
Hönig, S. F., Kishimoto, M., Gandhi, P., et al. 2010, A&A, 515, A23
Hönig, S. F., Kishimoto, M., Tristram, K. R. W., et al. 2013, ApJ, 771, 87
Ichikawa, K., Packham, C., Ramos Almeida, C., et al. 2015, ApJ, 803, 57
Imanishi, M., Nguyen, D. D., Wada, K., et al. 2020, ApJ, 902, 99
Impellizzeri, C. M. V., Gallimore, J. F., Baum, S. A., et al. 2019, ApJ, 884, L28
Isbell, J. W., Burtscher, L., Asmus, D., et al. 2021, ApJ, 910, 104
Izumi, T., Wada, K., Fukushige, R., Hamamura, S., & Kohno, K. 2018, ApJ, 867, 48
Jacquet, E., & Krumholz, M. R. 2011, ApJ, 730, 116
Jensen, J. J., Hönig, S. F., Rakshit, S., et al. 2017, MNRAS, 470, 3071
Käufl, H. U., Kerber, F., Asmus, D., et al. 2015, The Messenger, 159, 15
Kerber, F., Käufl, H. U., Tristram, K., et al. 2016, in Ground-based and Airborne Instrumentation for Astronomy VI, eds. C. J. Evans, L. Simard, H. Takami, SPIE Conf. Ser., 9908, 99080D
Kishimoto, M., Hönig, S. F., Beckert, T., & Weigelt, G. 2007, A&A, 476, 713
Koss, M., Trakhtenbrot, B., Ricci, C., et al. 2017, ApJ, 850, 74
Krolik, J. H. 2007, ApJ, 661, 52
Lagage, P. O., Pel, J. W., Authier, M., et al. 2004, The Messenger, 117, 12
Leftley, J. H., Hönig, S. F., Asmus, D., et al. 2019, ApJ, 886, 55
López-Gonzaga, N., Jaffe, W., Burtscher, L., Tristram, K. R. W., & Meisenheimer, K. 2014, A&A, 565, A71
López-Gonzaga, N., Burtscher, L., Tristram, K. R. W., Meisenheimer, K., & Schartmann, M. 2016, A&A, 591, A47
Lopez-Rodriguez, E., Fuller, L., Alonso-Herrero, A., et al. 2018, ApJ, 859, 99
Lopez-Rodriguez, E., Alonso-Herrero, A., García-Burillo, S., et al. 2020, ApJ, 893, 33
Lyu, J., & Rieke, G. H. 2021, ApJ, 912, 126
Maiolino, R., & Rieke, G. H. 1995, ApJ, 454, 95
Martínez-Paredes, M., González-Martín, O., Esparza-Arredondo, D., et al. 2020, ApJ, 890, 152
Martini, P., Regan, M. W., Mulchaey, J. S., & Pogge, R. W. 2003, ApJS, 146, 353
Mason, R. E., Lopez-Rodriguez, E., Packham, C., et al. 2012, AJ, 144, 11
Müller-Sánchez, F., Prieto, M. A., Hicks, E. K. S., et al. 2011, ApJ, 739, 69
Nenkova, M., Sirocky, M. M., Ivezić, Ž., & Elitzur, M. 2008a, ApJ, 685, 147
Nenkova, M., Sirocky, M. M., Nikutta, R., Ivezić, Ž., & Elitzur, M. 2008b, ApJ, 685, 160
Netzer, H. 2015, ARA&A, 53, 365
Nikutta, R., Lopez-Rodriguez, E., Ichickawa, K., et al. 2021, ApJ, submitted
Ogawa, S., Ueda, Y., Tanimoto, A., & Yamada, S. 2021, ApJ, 906, 84

Packham, C., Radomski, J. T., Roche, P. F., et al. 2005a, ApJ, 618, L17
Packham, C., Telesco, C. M., Hough, J. H., & Ftaclas, C. 2005b, in Rev. Mex. Astron. Astrofis. Conf. Ser., eds. A. M. Hidalgo-Gámez, J. J. González, J. M. Rodríguez Espinosa, & S. Torres-Peimbert, 24, 7
Packham, C., Honda, M., Chun, M., et al. 2018, in Ground-based and Airborne Instrumentation for Astronomy VII, eds. C. J. Evans, L. Simard, H. Takami, SPIE Conf. Ser., 10702, 10702A0
Pasetto, A., González-Martín, O., Esparza-Arredondo, D., et al. 2019, ApJ, 872, 69
Pérez-Torres, M., Mattila, S., Alonso-Herrero, A., Aalto, S., & Efstathiou, A. 2021, A&ARv, 29, 2
Phillips, M. M. 1979, ApJ, 227, L121
Pier, E. A., & Krolik, J. H. 1992a, ApJ, 401, 99
Pier, E. A., & Krolik, J. H. 1992b, ApJ, 399, L23
Pier, E. A., & Krolik, J. H. 1993, ApJ, 418, 673
Radomski, J. T., Piña, R. K., Packham, C., et al. 2003, ApJ, 587, 117
Ramos Almeida, C., & Ricci, C. 2017, Nat. Astron., 1, 679
Ramos Almeida, C., Levenson, N. A., Rodríguez Espinosa, J. M., et al. 2009, ApJ, 702, 1127
Ramos Almeida, C., Levenson, N. A., Alonso-Herrero, A., et al. 2011, ApJ, 731, 92
Ricci, C., Trakhtenbrot, B., Koss, M. J., et al. 2017a, ApJS, 233, 17
Ricci, C., Trakhtenbrot, B., Koss, M. J., et al. 2017b, Nature, 549, 488
Rieke, G. H., Wright, G. S., Böker, T., et al. 2015, PASP, 127, 584
Ruschel-Dutra, D., Pastoriza, M., Riffel, R., Sales, D. A., & Winge, C. 2014, MNRAS, 438, 3434
Schartmann, M., Meisenheimer, K., Camenzind, M., et al. 2008, A&A, 482, 67
Schartmann, M., Wada, K., Prieto, M. A., Burkert, A., & Tristram, K. R. W. 2014, MNRAS, 445, 3878
Schmitt, H. R., Donley, J. L., Antonucci, R. R. J., Hutchings, J. B., & Kinney, A. L. 2003, ApJS, 148, 327
Siebenmorgen, R., Heymann, F., & Efstathiou, A. 2015, A&A, 583, A120
Stalevski, M., Fritz, J., Baes, M., Nakos, T., & Popović, L. Č. 2012, MNRAS, 420, 2756
Stalevski, M., Asmus, D., & Tristram, K. R. W. 2017, MNRAS, 472, 3854
Suganuma, M., Yoshii, Y., Kobayashi, Y., et al. 2006, ApJ, 639, 46
Tanimoto, A., Ueda, Y., Odaka, H., et al. 2019, ApJ, 877, 95
Tanimoto, A., Ueda, Y., Odaka, H., et al. 2020, ApJ, 897, 2
Tazaki, R., & Ichikawa, K. 2020, ApJ, 892, 149
Telesco, C. M., Pina, R. K., Hanna, K. T., et al. 1998, in Infrared Astronomical Instrumentation, ed. A. M. Fowler, SPIE Conf. Ser., 3354, 534
Telesco, C. M., Ciardi, D., French, J., et al. 2003, in Instrument Design and Performance for Optical/Infrared Ground-based Telescopes, eds. M. Iye, A. F. M. Moorwood, SPIE Conf. Ser, 4841, 913
Thatte, N., Tecza, M., Schnetler, H., et al. 2021, The Messenger, 182, 7
Thomas, A. D., Dopita, M. A., Shastri, P., et al. 2017, ApJS, 232, 11
Tomono, D., Doi, Y., Usuda, T., & Nishimura, T. 2001, ApJ, 557, 637
Tristram, K. R. W., Burtscher, L., Jaffe, W., et al. 2014, A&A, 563, A82
Urry, C. M., & Padovani, P. 1995, PASP, 107, 803
Vasudevan, R. V., Fabian, A. C., Gandhi, P., Winter, L. M., & Mushotzky, R. F. 2010, MNRAS, 402, 1081
Venanzi, M., Hönig, S., & Williamson, D. 2020, ApJ, 900, 174
Venturi, G., Nardini, E., Marconi, A., et al. 2018, A&A, 619, A74
Véron-Cetty, M. P., & Véron, P. 2006, A&A, 455, 773
Wada, K., Schartmann, M., & Meijerink, R. 2016, ApJ, 828, L19
Wada, K., Yonekura, K., & Nagao, T. 2018, ApJ, 867, 49
Walton, D. J., Reis, R. C., & Fabian, A. C. 2010, MNRAS, 408, 601
Williamson, D., Hönig, S., & Venanzi, M. 2019, ApJ, 876, 137
Williamson, D., Hönig, S., & Venanzi, M. 2020, ApJ, 897, 26
Wold, M., & Galliano, E. 2006, MNRAS, 369, L47
Wright, G. S., Wright, D., Goodson, G. B., et al. 2015, PASP, 127, 595
Zhang, D., Davis, S. W., Jiang, Y.-F., & Stone, J. M. 2018, ApJ, 854, 110

[1] Centro de Astrobiología (CAB, CSIC-INTA), ESAC Campus, 28692 Villanueva de la Cañada, Madrid, Spain
e-mail: aalonso@cab.inta-csic.es
[2] Observatorio de Madrid, OAN-IGN, Alfonso XII, 3, 28014 Madrid, Spain
[3] Department of Physics & Astronomy, University of Southampton, Hampshire, SO17 1BJ Southampton, UK
[4] Department of Physics, University of Oxford, Oxford OX1 3RH, UK
[5] Instituto de Astrofísica de Canarias, Calle Vía Láctea, s/n, 38205 La Laguna, Tenerife, Spain
[6] Departamento de Astrofísica, Universidad de La Laguna, 38205 La Laguna, Tenerife, Spain
[7] Instituto de Radioastronomía y Astrofísica (IRyA-UNAM), 3-72 (Xangari), 8701 Morelia, Mexico
[8] Kavli Institute for Particle Astrophysics and Cosmology (KIPAC), Stanford University, Stanford, CA 94305, USA
[9] Astronomical Institute, Academy of Sciences, Bôcní II 1401, 14131 Prague, Czechia
[10] Leiden Observatory, PO Box 9513, 2300 RA Leiden, The Netherlands
[11] LERMA, Observatoire de Paris, Collège de France, PSL University, CNRS, Sorbonne University, Paris, France
[12] Max-Planck-Institut für Extraterrestrische Physik, Postfach 1312, 85741 Garching, Germany
[13] Institute of Astrophysics, Foundation for Research and Technology-Hellas, 71110 Heraklion, Greece
[14] Department of Physics & Astronomy, University of Alaska Anchorage, Anchorage, AK 99508-4664, USA
[15] INAF – Osservatorio Astrofisico di Arcetri, Largo Enrico Fermi 5, 50125 Firenze, Italy
[16] Frontier Research Institute for Interdisciplinary Sciences, Tohoku University, Sendai 980-8578, Japan
[17] Astronomical Institute, Tohoku University, 6-3 Aramaki, Aoba-ku, Sendai 980-8578, Japan
[18] National Astronomical Observatory of Japan, National Institutes of Natural Sciences (NINS), 2-21-1 Osawa, Mitaka, Tokyo 181-8588, Japan
[19] Department of Astronomy, School of Science, The Graduate University for Advanced Studies, SOKENDAI, Mitaka, Tokyo 181-8588, Japan
[20] National Astronomical Observatory of Japan, 2-21-1 Osawa, Mitaka, Tokyo 181-8588, Japan
[21] Department of Astronomical Science, The Graduate University for Advanced Studies, SOKENDAI, 2-21-1 Osawa, Mitaka, Tokyo 181-8588, Japan
[22] Centro de Astrobiología (CAB, CSIC-INTA), Carretera de Ajalvir, 28850 Torrejón de Ardoz, Madrid, Spain
[23] Space Telescope Science Institute, Baltimore, MD 21218, USA
[24] The University of Texas at San Antonio, One UTSA Circle, San Antonio, TX 78249, USA
[25] Núcleo de Astronomía de la Facultad de Ingeniería, Universidad Diego Portales, Av. Ejército Libertador 441, Santiago, Chile
[26] Kavli Institute for Astronomy and Astrophysics, Peking University, Beijing 100871, PR China
[27] Centre for Extragalactic Astronomy, Department of Physics, Durham University, South Road, Durham DH1 3LE, UK
[28] LESIA, Observatoire de Paris, PSL Research University, CNRS, Sorbonne Universités, UPMC Univ. Paris 06, Univ. Paris Diderot, Sorbonne Paris Cité, 5 Place Jules Janssen, 92190 Meudon, France
[29] Astronomical Observatory, Volgina 7, 11060 Belgrade, Serbia
[30] Sterrenkundig Observatorium, Universiteit Ghent, Krijgslaan 281-S9, Ghent 9000, Belgium
[31] Kagoshima University, Graduate School of Science and Engineering, Kagoshima 890-0065, Japan
[32] Ehime University, Research Center for Space and Cosmic Evolution, Matsuyama 790-8577, Japan
[33] Hokkaido University, Faculty of Science, Sapporo 060-0810, Japan

Appendix A: Additional CAT3D-WIND model images

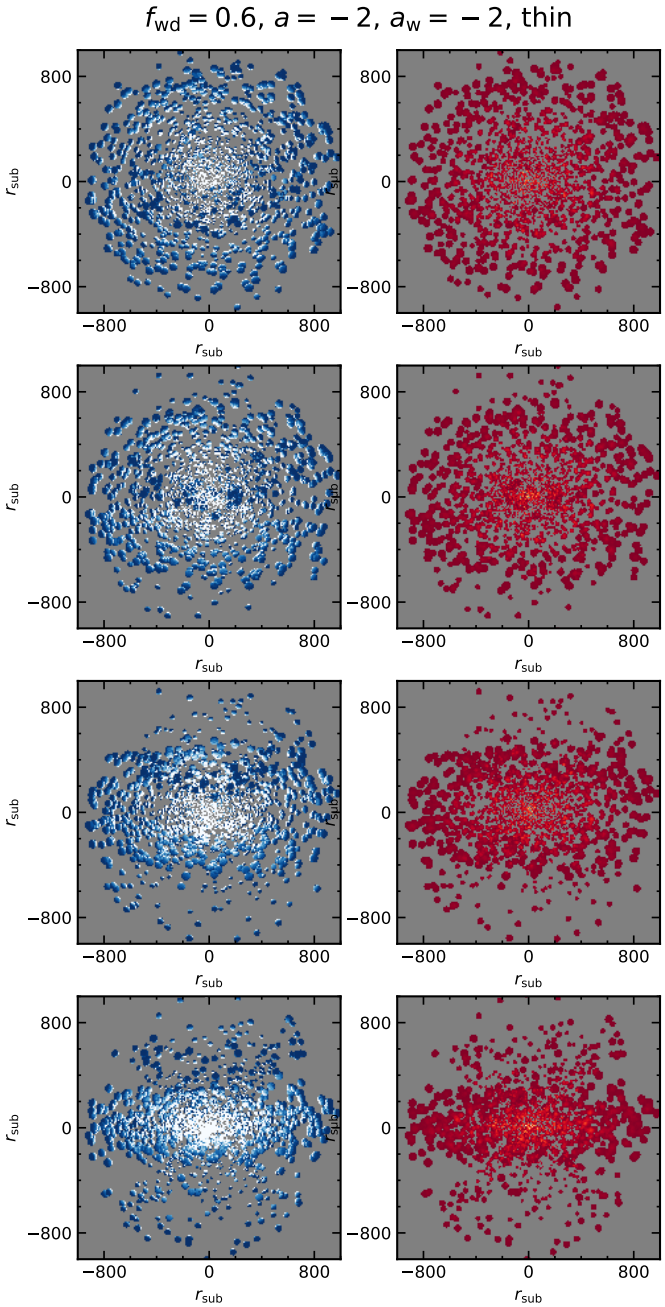

Fig. A.1. CAT3D-WIND model images for a "thin" geometry and f_{wd} = 0.6 at 8 µm (in blue colors, *left panels*) and 700 µm (in orange colors, *right panels*) for a compact disk – wind ($a = -2$, $a_w = -2$). *From top to bottom*: the inclinations are 30° (nearly face-on disk), 45°, 60°, and 75° (nearly edge-on disk).

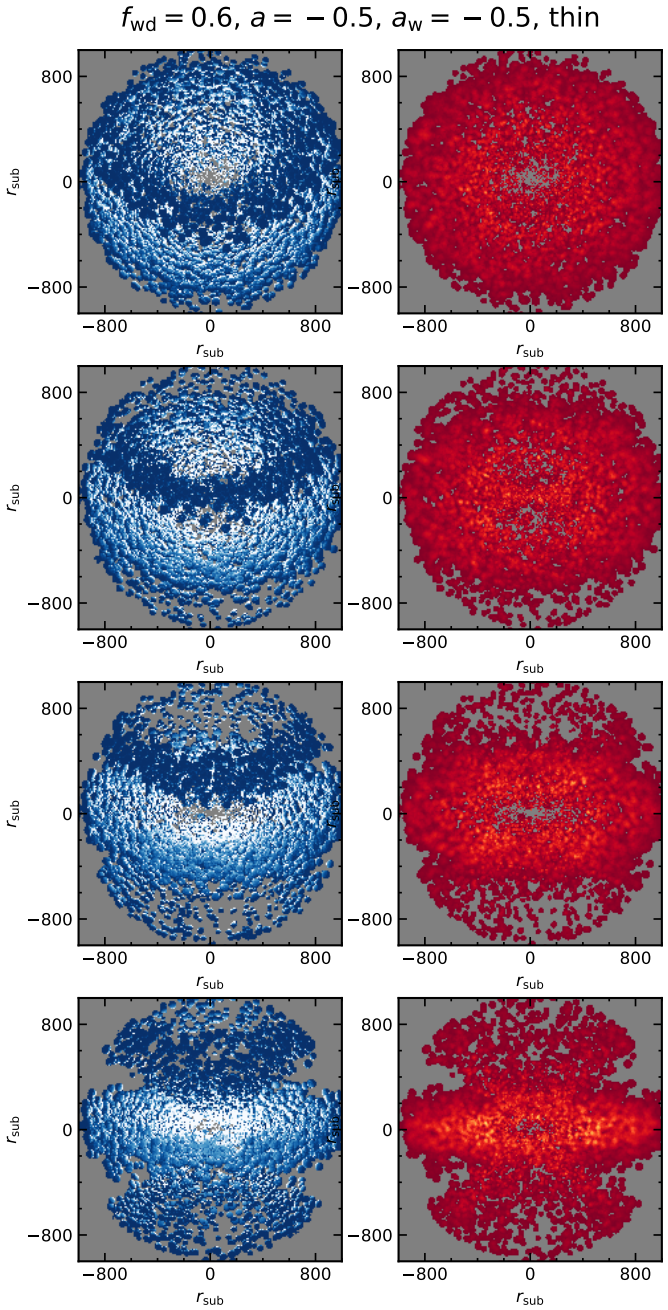

Fig. A.2. CAT3D-WIND model images for a "thin" geometry and f_{wd} = 0.6 at 8 µm (in blue colors, *left panels*) and 700 µm (in orange colors, *right panels*) for an extended disk – wind ($a = -0.5$, $a_w = -0.5$). *From top to bottom*: the inclinations are 30° (nearly face-on disk), 45°, 60°, and 75° (nearly edge-on disk).

We show in this appendix additional CAT3D-WIND mid- and far-IR model images for the compact disk – compact wind and extended disk – extended wind configurations for the "thin" and "thick" geometries and f_{wd} = 0.6 in Figs. A.1–A.4, respectively. We also show for the "thin" geometry and the four disk and wind configurations the mid- and far-IR model images for a wind-to-disk ratio of f_{wd} = 1.2 in Figs. A.5–A.8. All these images were discussed briefly in Sects. 5.3 and 5.4.

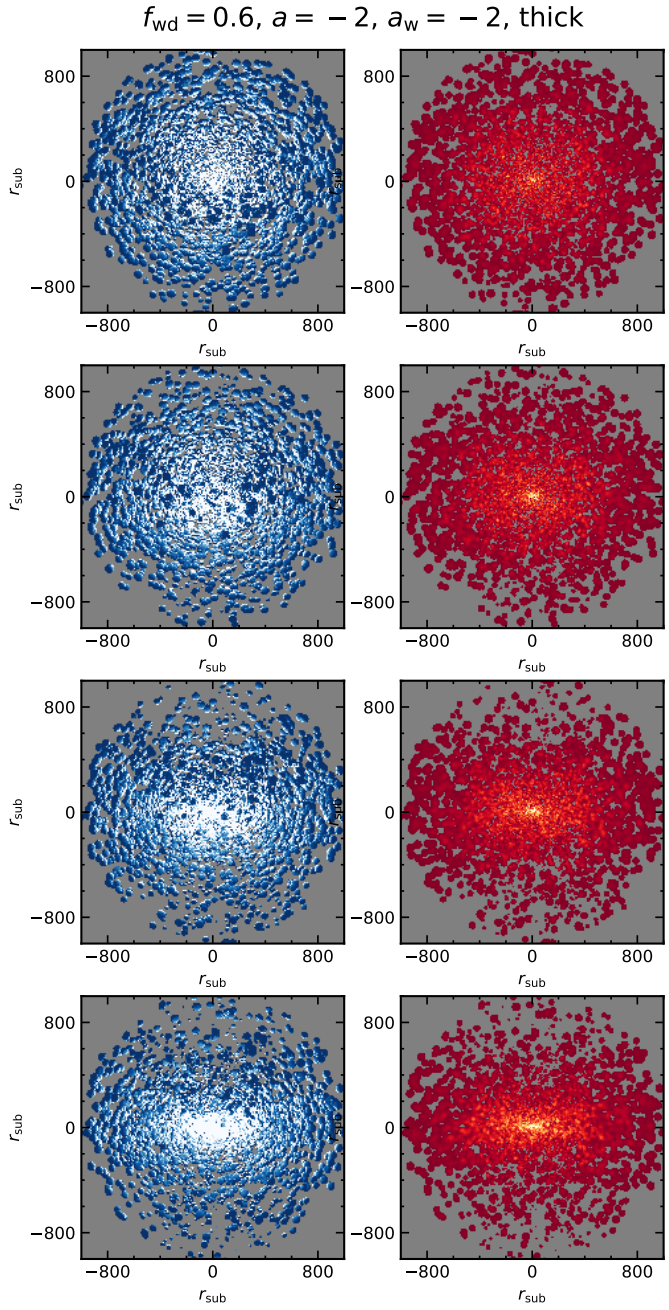

Fig. A.3. CAT3D-WIND model images for a "thick" geometry and $f_{wd} = 0.6$ at 8 µm (in blue colors, *left panels*) and 700 µm (in orange colors, *right panels*) for a compact disk – wind ($a = -2$, $a_w = -2$). *From top to bottom*: the inclinations are 30° (nearly face-on disk), 45°, 60°, and 75° (nearly edge-on disk).

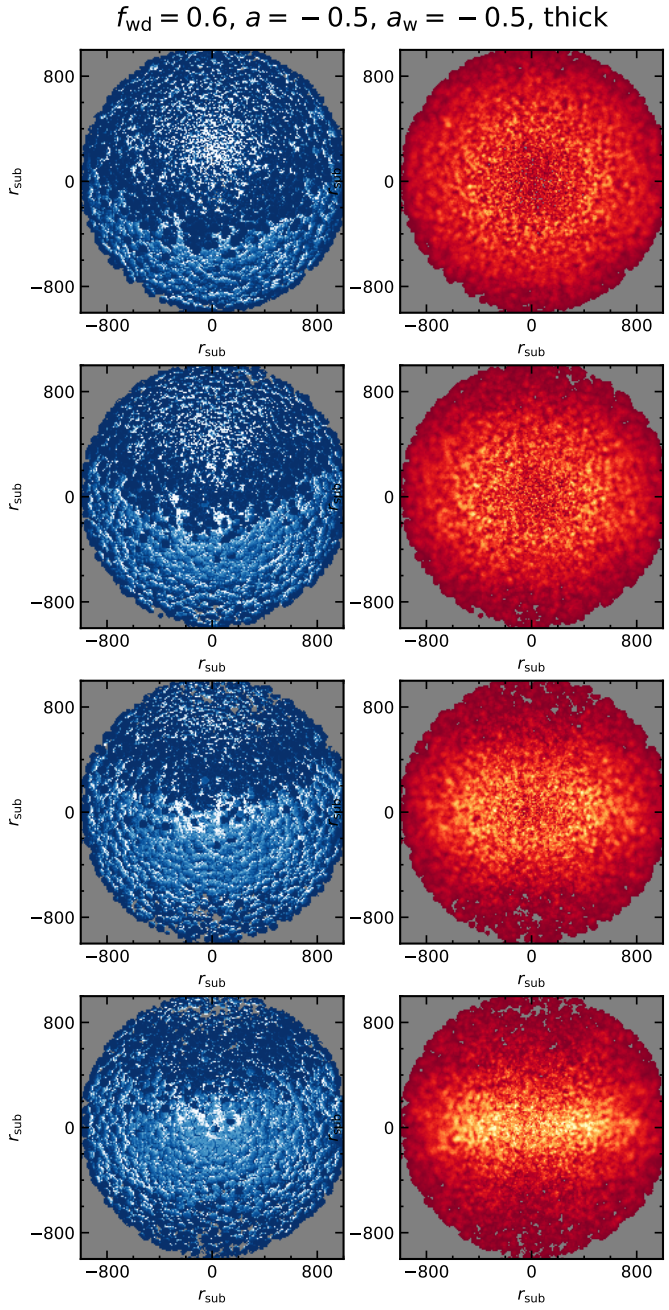

Fig. A.4. CAT3D-WIND model images for a "thick" geometry and $f_{wd} = 0.6$ at 8 µm (in blue colors, *left panels*) and 700 µm (in orange colors, *right panels*) for an extended disk – wind ($a = -0.5$, $a_w = -0.5$). *From top to bottom*: the inclinations are 30° (nearly face-on disk), 45°, 60°, and 75° (nearly edge-on disk).

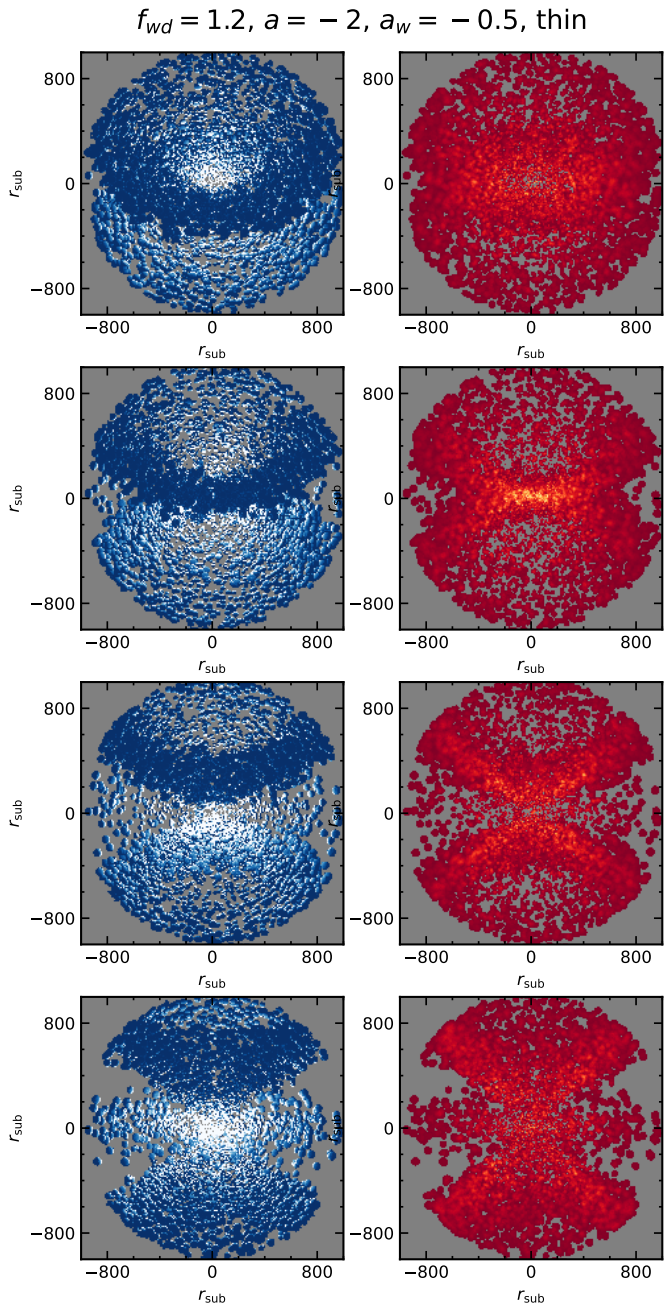

Fig. A.5. CAT3D-WIND model images for a "thin" geometry and f_{wd} = 1.2 at 8 µm (in blue colors, *left panels*) and 700 µm (in orange colors, *right panels*) for a compact disk – extended wind configuration. *From top to bottom*: the inclinations are 30° (nearly face-on disk), 45°, 60°, and 75° (nearly edge-on disk).

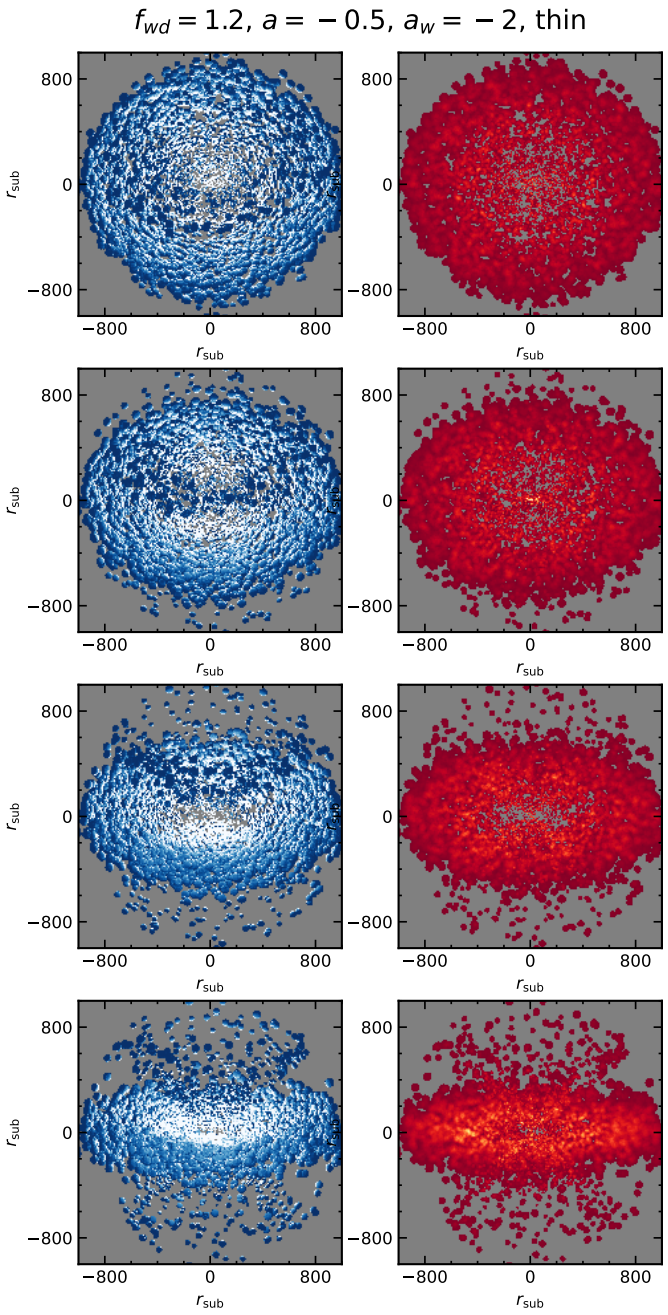

Fig. A.6. CAT3D-WIND model images for a "thin" geometry and f_{wd} = 1.2 at 8 µm (in blue colors, *left panels*) and 700 µm (in orange colors, *right panels*) for an extended disk – compact wind configuration. *From top to bottom*: the inclinations are 30° (nearly face-on disk), 45°, 60°, and 75° (nearly edge-on disk).

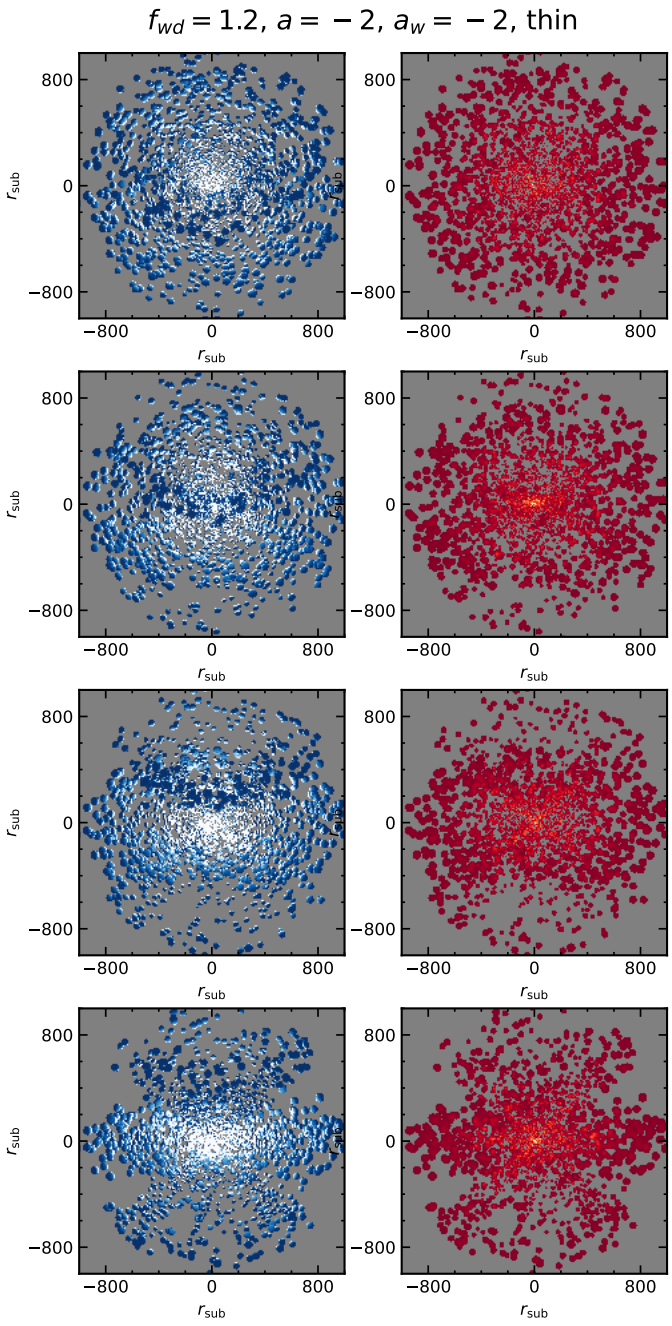

Fig. A.7. CAT3D-WIND model images for a "thin" geometry and f_{wd} = 1.2 at 8 µm (in blue colors, *left panels*) and 700 µm (in orange colors, *right panels*) for a compact disk – compact wind configuration. *From top to bottom*: the inclinations are 30° (nearly face-on disk), 45°, 60°, and 75° (nearly edge-on disk).

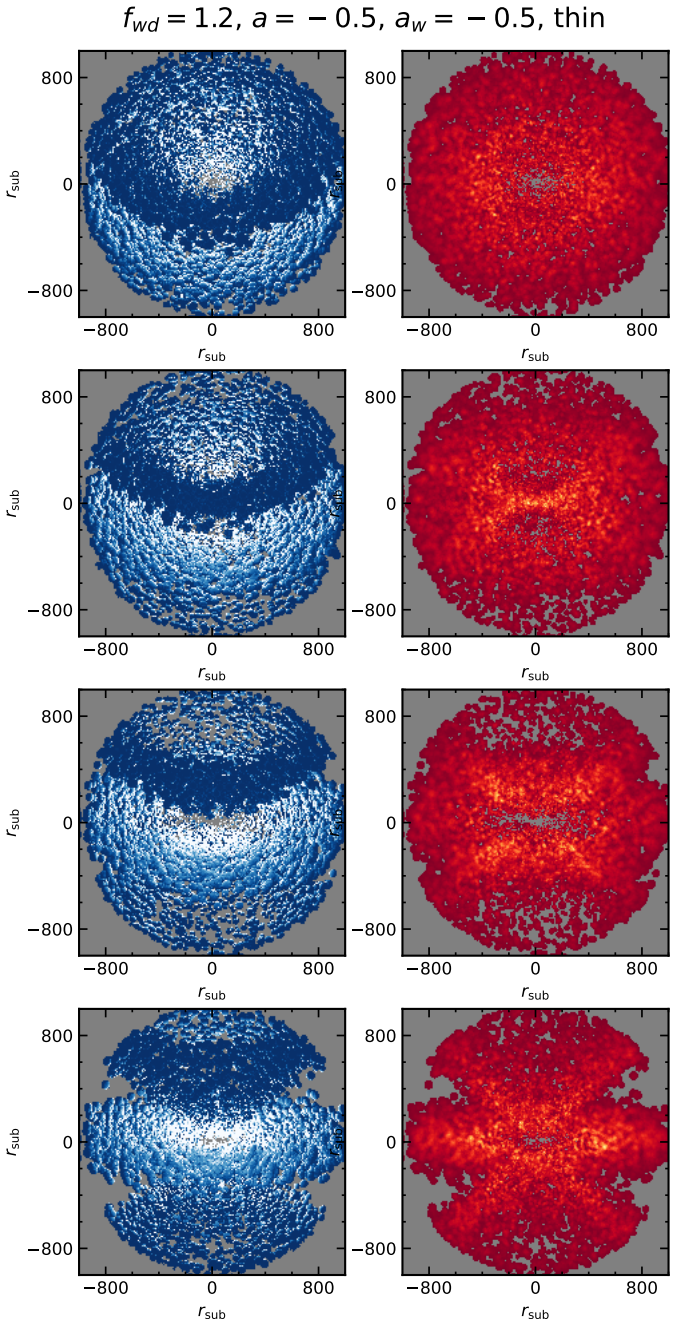

Fig. A.8. CAT3D-WIND model images for a "thin" geometry and f_{wd} = 1.2 at 8 µm (in blue colors, *left panels*) and 700 µm (in orange colors, *right panels*) for an extended disk – extended wind configuration. *From top to bottom*: the inclinations are 30° (nearly face-on disk), 45°, 60°, and 75° (nearly edge-on disk).